

Determining the Mass of Saturn's Satellite, Daphnis

Aaron Bauer, Paul Thomas, Department of Physics and Astronomy
University of Wisconsin, Eau Claire

October 4, 2010

Abstract

In 2005, the Cassini spacecraft captured a picture of the Keeler gap in Saturn's A-ring that showed Saturn's satellite Daphnis surrounded by wave-like disturbances in the inner and outer edges of the gap. We present a numerical model for the formation of these waves as a result of the gravitational interaction between Daphnis and particles of the A-ring. The wavy motion depends highly on the mass of Daphnis and the gravitational force it exerts on the nearby ring particles. By comparing the amplitude of the waves seen in the Cassini images to those produced in a numerical simulation, it is possible to accurately determine the mass of Daphnis. Our analysis shows a mass of $15.0 \pm .5 \times 10^{13}$ kg.

Keywords: Cassini images, centrifugal force, Coriolis force, Daphnis, finite difference method, Keeler Gap, orbits, Newtonian mechanics, Newton's law of universal gravitation, rotating reference frame, Saturn, shepherding moon, waves

1 Introduction

One of the most interesting planetary ring dynamics is the phenomena of shepherding. Shepherding is the process by which a satellite shapes a ring by changing the eccentricity of the orbits for each ring particle by gravitational forces. By analyzing the shepherding effects, one can deduce certain physical information about the shepherding satellites. One particular case is Daphnis, a moon of Saturn, whose mass can be deduced by looking at trajectories of the particles it "herds."

Cassini images revealed in 2005 a peculiar structure of the rings bordering the Keeler Gap, a 35-km gap in Saturn's A-ring [1]. It was later determined that there resided a satellite inside the gap (Daphnis) which was the cause of the ring structure. Near the satellite, the bordering rings took on a wave-like appearance, while further from the satellite these oscillations dampened out due to particle collisions, and eventually attained their

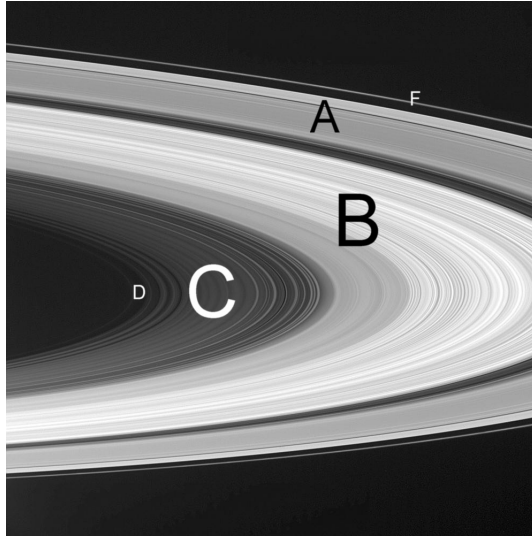


Figure 1: Saturn's Ring Systems, as imaged by the NASA/ESA Cassini spacecraft, see ref [3].

conventional orbits. The images used here can be accessed at the online Cassini Photojournal at photojournal.jpl.nasa.gov.

The goal of the research being presented here is to compare a numerical simulation of the wave-like structure to the images retrieved by the Cassini spacecraft to determine the mass of Daphnis. Currently, there are large uncertainties in the value for the mass of Daphnis. The Cassini Imaging team estimates that Daphnis is 7 km across, so we can determine a range of masses that we should expect that of Daphnis to fall within [2]. The moon's mass, m , may be written $m = \rho V$, where the density, ρ , ranges from .5 g/cm³ to 2 g/cm³, which includes the densities of plausible materials that Daphnis may be composed of (eg. ice). The range of masses is 5 - 50 x 10¹³ kg.

The structure of the paper will be as follows: first (section 2), an in-depth look at how the model works, along with any assumptions that were made in the building of the model and their justifications; second (section 3), an explanation of how the Cassini images are analyzed and how they will be compared to the model; third (section 4), the results of the simulations; finally (section 5), a conclusion with an analysis of the validity of the results.

2 The Model

In this problem, it is convenient to work in a non-inertial reference frame. We define a coordinate system that is centered on Saturn, but rotates as to keep Daphnis on the y-axis. This requires us to consider those forces that would be fictitious in an inertial reference frame. Of those, we consider only the centrifugal and Coriolis forces. Another feature of our model is that it uses a viewing window to constrict our view to a small region around Daphnis. As particles stream out one side of the window, identical, undisturbed particles stream in the other side. For a more in-depth analysis of this local simulation method, see reference [4]. This allows us to see the rings near Daphnis in greater detail and it cuts down the computation time since we are uninterested in calculating the motion of the majority of the ring.

As it is, the complexity of this problem is much too high for the purpose of this research, so we will make some assumptions about the system to make it simpler. First, the ring particles are of negligible mass, and therefore, do not exert any detectable gravitational forces on one another. More broadly, all particle-particle interactions among ring particles are ignored. While obviously present in actuality, these forces are miniscule in magnitude compared to the fictitious non-inertial forces and the gravitational forces from Saturn and Daphnis. The gravitational force acting on the ring particles due to the mass of the ring interior to their orbits has also been neglected in this calculation. The total mass of the rings is of the order of 6.6×10^{-8} times that of Saturn, and therefore has a negligible effect on the orbits of the ring particles [7]. One other assumption is that the ring particles and satellites are confined to travel in two dimensions. The vertical height of the rings is around 10 km while the radial width is in the hundreds of kilometers, so it is justifiable to assume only two-dimensional rings.

Our numerical model employs the Finite Difference Method for approximating the solutions to the differential equations of motion for each ring particle. Given initial velocities and positions of the individual particles, we were able to calculate their positions and velocities a time ΔT later. It is important to explicitly define a ΔT that is optimized for a

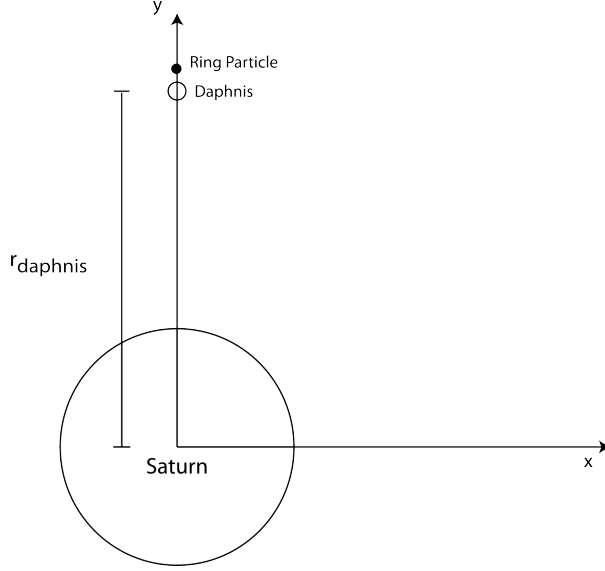


Figure 2: Coordinate System viewed from +z-axis. The coordinate system shown rotates in a counter-clockwise sense as Daphnis revolves around Saturn. In our reference frame, Daphnis stays on the y-axis; however, the ring particle will have variable x and y components.

given simulation. If ΔT is too short, computation time is wasted, while if ΔT is too large, the system might become unstable and small-scale details may be skipped over.

There are four forces acting upon each ring particle in our model: Saturn's gravity, Daphnis' gravity, the Coriolis force, and the centrifugal force. Since the particles are of negligible mass, we cannot find the magnitudes of the forces, but we can find the magnitudes of the forces per unit mass. With our rotating reference frame, Daphnis always lies on the y-axis, with the origin at the center of Saturn.

$$a_{net,x} = \frac{F_{net,x}}{m} = \frac{1}{m}(F_{cor,x} + F_{cf,x} + F_{grav,sat,x} + F_{grav,shep,x}) \quad (1)$$

$$\frac{F_{cor,x}}{m} = 2\omega v_y \quad (2)$$

$$\frac{F_{cf,x}}{m} = \omega^2 x \quad (3)$$

$$\frac{F_{grav,sat,x}}{m} = \frac{-GM_{saturn}x}{(x^2 + y^2)^{3/2}} \quad (4)$$

$$\frac{F_{grav,shep,x}}{m} = \frac{-GM_{daphnis}x}{(x^2 + (y - r_{daphnis})^2)^{3/2}} \quad (5)$$

$$a_{net,y} = \frac{F_{net,y}}{m} = \frac{1}{m}(F_{cor,y} + F_{cf,y} + F_{grav,sat,y} + F_{grav,shep,y}) \quad (6)$$

$$\frac{F_{cor,y}}{m} = -2\omega v_x \quad (7)$$

$$\frac{F_{cf,y}}{m} = \omega^2 y \quad (8)$$

$$\frac{F_{grav,sat,y}}{m} = \frac{-GM_{saturn}y}{(x^2 + y^2)^{3/2}} \quad (9)$$

$$\frac{F_{grav,shep,y}}{m} = \frac{-GM_{daphnis}(y - r_{daphnis})}{(x^2 + (y - r_{daphnis})^2)^{3/2}} \quad (10)$$

where G is the gravitational constant, M is a mass, x and y are particle positions, ω is the angular velocity at which the reference frame rotates (1.19×10^{-4} rad/s), and $r_{daphnis}$ is the distance from Saturn to Daphnis (1.36504×10^8 m). With these accelerations we can compute new velocities.

$$v_x = a_{net,x} \Delta T \quad (11)$$

$$v_y = a_{net,y} \Delta T \quad (12)$$

With these velocities we can compute new particle positions; ΔT was taken to be 25 sec, or .049 percent of the orbital period of Daphnis;

$$x = v_x \Delta T \quad (13)$$

$$y = v_y \Delta T \quad (14)$$

3 Image Analysis and Comparison

In the model, the mass of Daphnis is a free parameter, and running the simulations with different masses results in wave amplitudes of different magnitudes. The goal here is to find the amplitude, in meters, of the first wave oscillation from the Cassini images. The simulation is then run for a wide range of masses for Daphnis, creating a trendline and, in

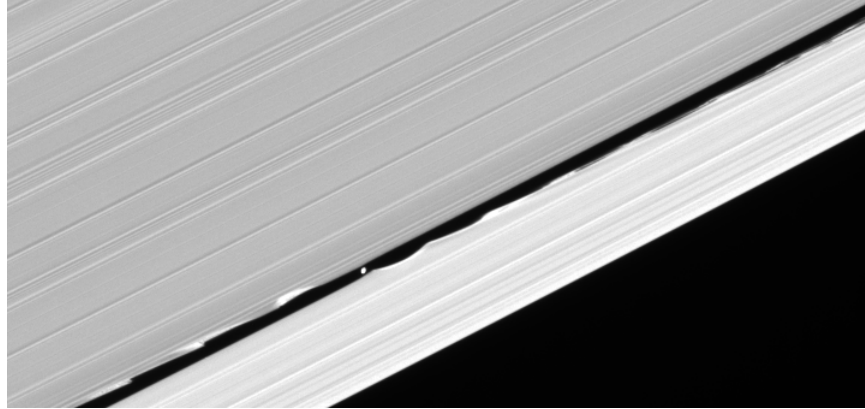


Figure 3: NASA/ESA Cassini spacecraft Image PIA08319, see ref [2].

extension, an equation for wave amplitude vs. mass. From this equation, we can extrapolate the mass of Daphnis which matches what it seen from the images most closely.

The chosen Cassini image was PIA08319. The task now is to find the scaling of the image in km/pixel. We will use two independent methods to accomplish this, thus improving accuracy. The first method involves using the known width (35 km) of the Keeler Gap to find the resolution of the image. From the image, the Keeler Gap is 10.6 pixels across, on average.

$$\text{Resolution} = \frac{35 \text{ km}}{10.6 \text{ pix}} = 3.3 \text{ km/pixel} \quad (15)$$

This method results in a resolution of 3.3 km/pixel.

The second method is more involved and uses information about the location of the spacecraft relative to the ring plane when the image was taken and specifications of the lens of the camera. The image was taken with a wide-angle lens that has a viewing-angle of 0.006109 radians. The CCD has an array of 1024 pixels by 1024 pixels, so each image taken with that camera has a width of 1024 pixels [5]. The last piece of information needed is the distance between Cassini and Daphnis, which is 3.25×10^8 m [2]. Using the arc-length formula,

$$s = \theta r \quad (16)$$

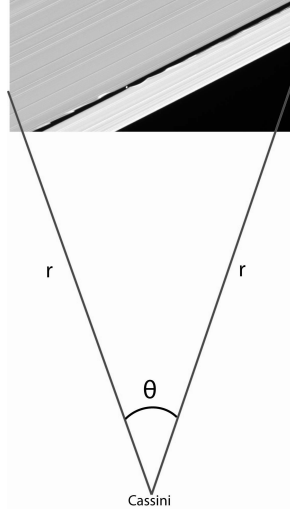


Figure 4: Geometry used to determine resolution.

$$s = (.006109 \text{ rad})(3.25 \times 10^8 \text{ m}) \quad (17)$$

$$s = 1990 \text{ km} \quad (18)$$

where s is the distance across the image. As stated before, the camera takes images with resolutions 1024×1024 , thus the resolution (in km/pix) is $\frac{1990 \text{ km}}{1024 \text{ pix}} = 1.94 \text{ km}/\text{pix}$. However, this is assuming that Cassini is directly below the ring-plane, which it is not, so we must alter our result accordingly. We are given the information that Cassini is located 25 degrees below the ring plane [2]. In Figure 4, we wish to find the angle ϕ . We know the following: $\theta = 25^\circ$, $y = 1.36504 \times 10^8 \text{ m}$, $x = 3.25 \times 10^8 \text{ m}$. Using the law of sines,

$$\frac{y}{\sin \gamma} = \frac{x}{\sin \theta} \quad (19)$$

yielding,

$$\gamma = 10^\circ \quad (20)$$

From that, $\phi = 35^\circ$. From where Cassini is positioned, the wave amplitude appears smaller, thus we must divide the resolution by $\sin \phi$ to appropriately correct for point-of-view issues.

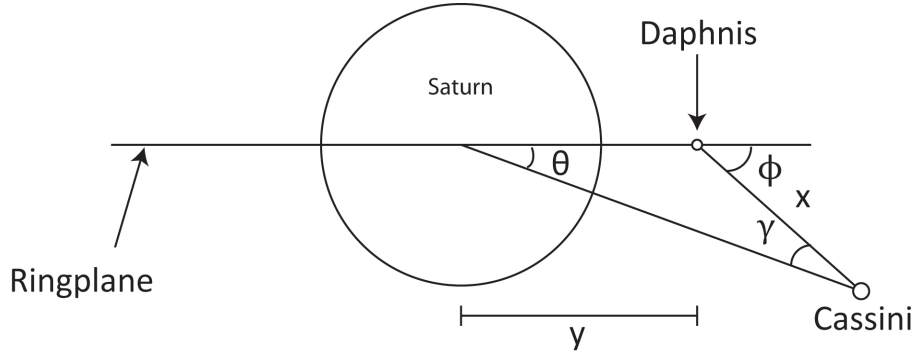


Figure 5: Geometrical representation of location of Cassini in relation to the ring plane of Saturn (not to scale).

This method results in a resolution of 3.38 km/pix using the following method. Taking an average of the two methods, we get a final resolution of 3.34 km/pixel for PIA08319. Now that we have an average, we must determine the number of pixels that make up the amplitude of the wave oscillation. To make the process simpler, instead we will find the number of pixels that make up the distance from the valley of the first wave to the peak of the next. By fitting a sinusoid to the pixel intensity vs. distance, we obtain a value of 5.0 pixels. Subpixel accuracy is obtained because of the number of pixels (~ 20) used to fit the curve. Multiplying that by our resolution, we end with a peak-to-valley value of 17 km.

4 The Results

Now that we have know the distance between a wave peak and valley, we can run the simulation to determine what Daphnis mass yields the same value. The simulation was run with masses ranging from 12 - 18 x 10^{13} kg and the peak-to-valley distance was measured, after which a Daphnis mass vs. amplitude plot was generated. A line was fit to the data yielding an equation for the trend. Solving for the mass by substituting the known ring amplitude yields a mass of Daphnis of 15 x 10^{13} kg. As shown in the figure above, there exists an upper limit on how massive Daphnis can be. For masses greater than 22×10^{13} kg, Daphnis exerts a gravitational force on the ring particles sufficient to remove them from the

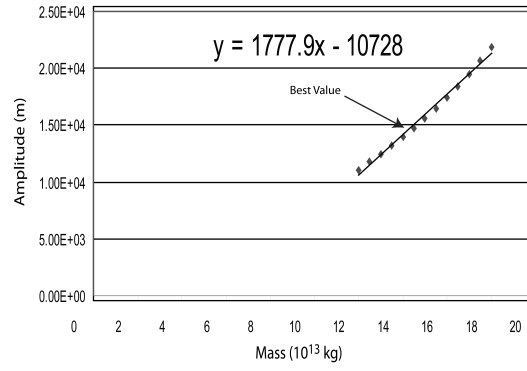


Figure 6: Ring amplitude vs. Daphnis mass from numerical model.

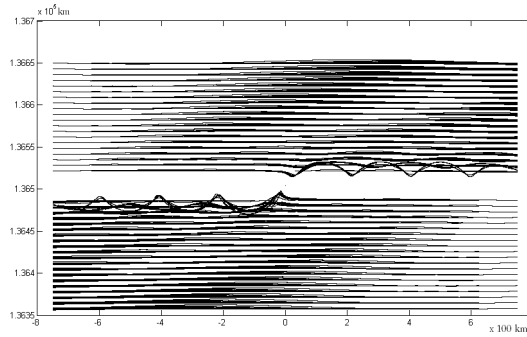


Figure 7: Resulting image from simulation when run with the correct Daphnis mass.

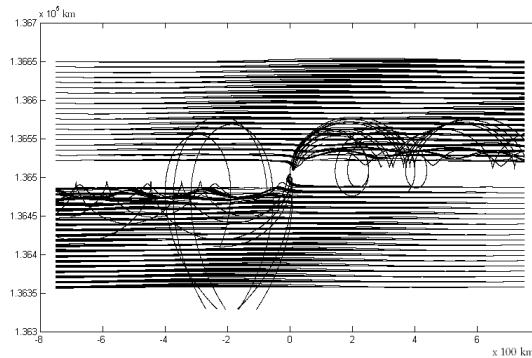


Figure 8: Resulting image from simulation when run at upper bound for Daphnis' mass.

edge of the A ring. This may account for the formation of the Keeler Gap.

Oldenhuis and Gunneman list the mass as 95×10^9 kg [6]. Running our simulation with that mass causes no discernible disturbances in the ring structure, which is evidence that a larger mass is needed.

5 Conclusion

We have completed our goal of determining the mass of Saturn's satellite, Daphnis. The full journey, however, is not yet finished. As stated earlier, certain assumptions were made to simplify the model; there were no particle-particle interactions among ring particles, both electrostatically and gravitationally, and we have yet to consider the particles moving in three dimensions. Removing these assumptions is the next step in creating a more accurate and realistic model.

References

- [1] USGS Gazetteer of Planetary Nomenclature.
<http://planetarynames.wr.usgs.gov/append8.html>. Last updated 2/09/09. Last consulted 6/05/09.
- [2] Cassini Photojournal: Image PIA08319. Cassini Imaging Team.
<http://photojournal.jpl.nasa.gov/catalog/PIA08319>. Last updated 11/28/06. Last consulted 6/05/09.
- [3] Cassini Photojournal: Image PIA06536. Cassini Imaging Team
<http://photojournal.jpl.nasa.gov/catalog/PIA06536>. Last updated 12/06/04. Last consulted 4/23/09.
- [4] J. Wisdom and S. Tremaine, Local Simulations of Planetary Rings. *Astronomical Journal* **95** (1988), pp. 925-940.

- [5] Imaging Science Subsystem. CICLOPS. <http://ciclops.org/iss/iss.php>. Last consulted 4/11/09.
- [6] R. Oldenhuis and J. Gunneman, Estimating the Density of Saturn's Moon Daphnis via its Shepherding Effect on Nearby Rings. *Earth and Planetary Observation Letters* **1** (2005), pp. 17-21.
- [7] L. Esposito, *Planetary Rings*, Cambridge University Press, 2006.

Effects of Hydrogen Flow Rate on Carbon Nanotube Growth

*Carolyn Reynolds**, *Binh Duong***, and *Supapan Seraphin***

**Dept. Optical Engineering, Norfolk State University, Norfolk, VA 23504; **Dept. Materials
Science and Engineering, University of Arizona, Tucson, AZ 85721*

Integrated Optics for Undergraduates (IOU)

an NSF-ERC sponsored Research Experience for Undergraduates (REU) Program

Abstract

This article presents the synthesis and characterization of carbon nanotubes (CNTs) on silicon substrates by chemical vapor deposition (CVD) at 900°C using methane and hydrogen flow rates. The variation of H₂ gas concentration and a set growth time of 15 minutes have a significant effect on distribution, morphology, internal structure, and electronic properties of the nanotubes. The transmission electron microscope (TEM) and state-of-the-art scanning electron microscope (SEM), equipped with Raman spectrometer, allowed us to obtain critical information on the morphology and chemical and electronic structures of the CNTs. The results revealed substantial quantity trends as hydrogen flow rate increased from 100 to 700 standard cubic centimeter per minute (sccm). At a constant CH₄ flow rate of 700 sccm and varied H₂ of 100 and 200 sccm, we observed that few CNTs were produced. Between H₂ flow rates of 300 and 400

sccm, the highest density of CNTs were grown; therefore, suggesting optimum growth conditions within that range. Increasing H₂ to 700 sccm, the amount of CNTs decreased. The results from this study will guide a production process to obtain high quantity and quality CNTs with desired properties.

Key Words: Carbon nanotubes (CNTs); chemical vapor deposition (CVD); hydrogen; methane; substrates; silicon

1. Introduction

Carbon nanotubes (CNTs) have become a forefront topic in research because of their unique electrical properties, chemically stable nature, and excellent mechanical strength. In addition, because of their efficient conductivity of electricity and heat, they are potentially useful in a wide variety of applications. A few of these applications include the making of solar cells, diodes, transistors, small electronic devices, high efficiency energy conversion fuel cells, smart materials, high performance sensors, and structural materials under extreme environment [4]. In order to fulfill the potential applications, extensive research must be carried out to ensure proper characteristics of these CNTs. This research is devoted to investigate the effects of hydrogen gas flow on the quantity and quality of CNTs.

In 1991, Sumio Iijima, a Japanese physicist, was credited for discovering CNTs [1]. Throughout research, there have been found to be three common variations of CNTs: single-walled (SWCNTs) double-walled (DWCNTs) and

multi-walled (MWCNTs). Single-walled CNTs can be described as a one-atom thick planar sheet of bonded carbon atoms (graphene) that are densely packed in a honeycomb crystal lattice. They can be categorized based upon their chiral vector or indices, (n, m) . If the pair of indices is $(n, 0)$, the structure is zigzag. If it is (n, n) , the structure is known to be armchair. All other combinations are chiral [6]. When CNTs have two layers of the planar sheets, they are called double-walled CNTs and more than two layers of graphene, multi-walled CNTs.

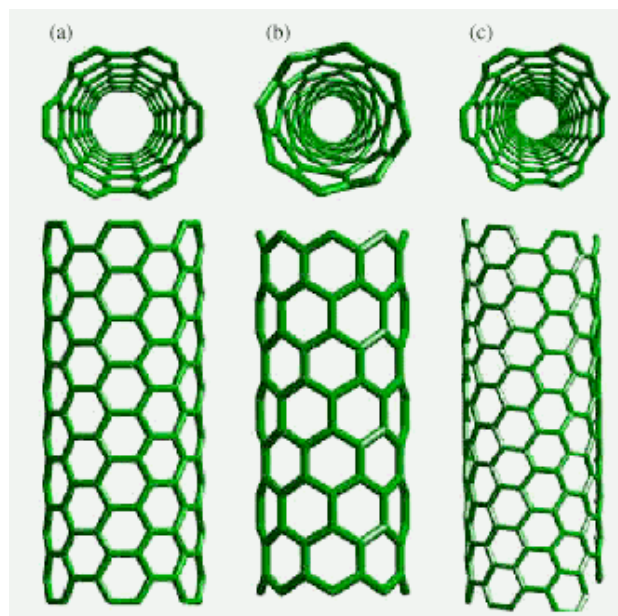


Figure 1 . (a) armchair, (b) zigzag, (c) chiral

Carbon nanotubes are grown using various methods. Some of these methods include chemical vapor deposition (CVD), arc discharge, and laser vaporization [5]. For this experiment, the CVD method is used mainly because it readily

allows a reproduction of trials, a large-scale nanotube production in a single trial, and an ease of process control.

Once the samples are grown, they are characterized using scanning electron microscopy (SEM), transmission electron microscopy (TEM), and Raman spectroscopy. From these characterization methods, details such as density, electrical properties, inner diameter, common variation (SW, DW, or MW-CNTs), and overall quality are determined.

2. Experimental Procedure

Carbon nanotubes were synthesized on silicon wafers using the chemical vapor deposition (CVD) system with gas flows of H₂, CH₄, and Ar. The parameters held constant for the experiment were: flow rates of 700 sccm (CH₄), 1000 sccm (Ar), baking time of 15 minutes, and furnace temperature of 900⁰C. The testing parameter was H₂ at 100, 200, 300, 400, 500, and 700 standard cubic centimeter per minute (sccm). A 0.1 mL sonicated catalyst solution of bis(acetylacetonato)-dioxomolybdenum (VI) [(C₅H₈O₂)₂ MoO₂], iron nitrate nonahydrate [Fe (NO₃)₃·9H₂O], aluminum oxide [Al₂O₃], and methanol was deposited on the wafers before being placed in the CVD gas flow system.

The established method for deposition of the catalyst solution was determined by comparing the outcomes of what we called the blow-drying and spinning methods. The first method consisted of dropping 0.1 mL of the solution onto the wafers, blow-drying the solution, and baking at 150⁰C for fifteen minutes. The

second method involved a spinner system in a clean room. The silicon wafer was placed on the chuck; 0.1 mL of the solution was deposited, and allowed to spin at different speeds for thirty seconds. The wafers/substrates were then ready to be used in the CVD system. The spinner method was first assumed to distribute the catalyst solution more evenly over the wafer compared to the first (blow-dry) method, but in testing, there was no major difference of catalyst dispersion seen between the two methods. The blow-drying method was therefore chosen to be used.

The operation of the CVD system started with Ar being released into the system until the furnace reached 900°C. H₂ and CH₄ were then allowed to flow simultaneously for fifteen minutes. Ar was opened again as the furnace was turned off to cool. The flow of Ar while cooling prevents the CNTs from being burned at such high temperatures. When the cooling was complete, the samples were ready to be removed for analysis. A total of four samples per condition were run in trial. Not all samples gave similar results so additional trials were run as needed.

Hitachi SEM S-4800, SEM S-4500, Hitachi TEM, and our state-of-the-art Renishaw Raman Spectroscopy, equipped on a Hitachi SEM S-3400 were the instruments used for analysis. To prepare the sample for TEM, the substrate must be submerged in isopropanol (IPA), scraped and bath-sonicated for approximately 30 minutes. The solution is then extracted using a syringe and placed on a copper

grid specifically designed for the TEM. The grids are left to air-dry. No additional preparation, such as coating, is needed for the SEM and Raman analysis.

3. Results and Discussion

All four samples from H₂ at 100 sccm showed very few CNTs as shown in Figure 2(a). Amorphous carbon was present on two of the four samples. The high CH₄ content decomposed to excessive amount of C atoms, which coated around the catalysts. This increased the activation energy of the CNT growth process, resulting in low density of CNTs. Three of the four samples for H₂ at 200 sccm showed little CNT growth (not shown in Figure 2). The fourth sample was highly inhomogeneous; some locations on the substrate possessed an abundance of CNTs while other areas had little CNT growth. All four samples for H₂: 300 sccm had an abundance of CNTs. These CNTs however had short branches and smaller outer diameters seen from SEM image in Figure 2(b). An abundance of CNTs was produced at H₂: 400 sccm on three of five samples. Around 300 and 400 sccm, the optimum growth condition is in close proximity to allow abundant production of CNTs. For H₂: 500 sccm, a small amount of CNTs was seen on the samples. Amorphous C was present also (not shown). Similar to H₂: 300 sccm, the CNTs had short branches. For all four samples at H₂: 700 sccm, low density of CNT was present. The CNTs also had short branches. As

the flow rate approached 700 sccm, the excessive presence of H atoms to C atoms produced few CNTs.

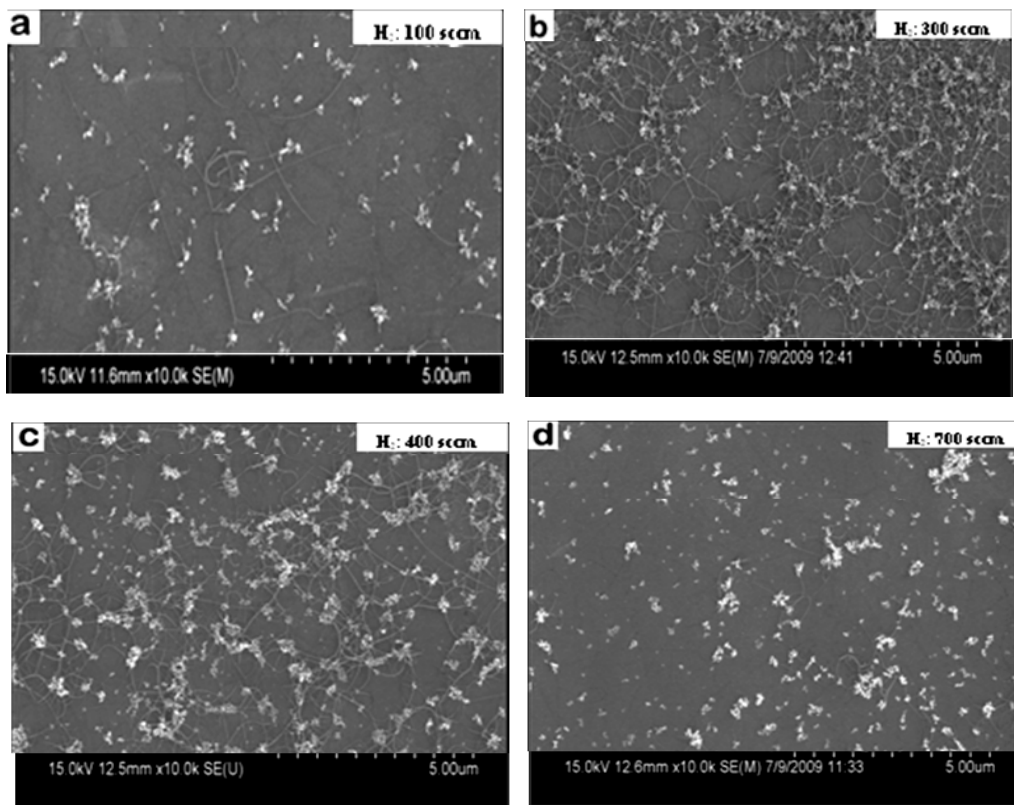


Figure 2. SEM images of CNTs grown at hydrogen flow rate of: (a) 100 sccm; (b) 300 sccm; (c) 400 sccm; (d) 700 sccm.

Figure 3 depicts TEM images of (a) graphite structure; (b) double-walled CNT; (c) multi-walled CNT. When images such as Fig. 3(a) are seen, the density of the CNTs is low. The graphitic structures are undesirable in our research. We prefer to have DWCNTs and MWCNTs as shown in (b) and (c).

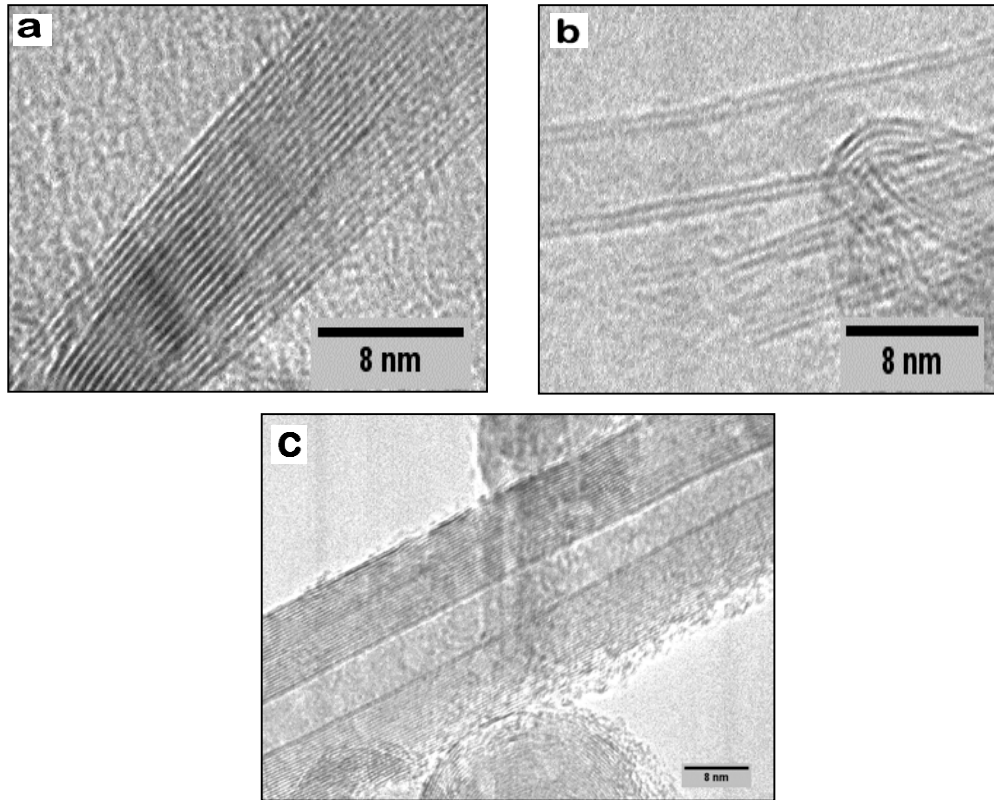


Figure 3 TEM images of: (a): Graphitic structure obtained from H₂ @ 300 sccm; (b): Double-walled CNT obtained from H₂ @ 200 sccm; (c): Multi-walled CNT obtained from H₂ @ 100 sccm

Raman spectroscopy was used to analyze the H₂: 200 sccm sample as shown in Figure 4. Using the Radial Breathing Mode (RBM) and its equation [5]:

$$\omega_{\text{RBM}} = \alpha / d_t$$

where ω is the RBM peak frequency, α is a constant equaling $248 \text{ nm}\cdot\text{cm}^{-1}$, the inner diameter (d_t) of the CNTs of this corresponding location was calculated. Calculating the diameter at all five extreme RBM peaks and taking the average, the average diameter equals 1.40 nm. The term D/G ratio commonly is used to represent the overall quality of the CNTs; quality as in the alignment and bonding regularity of the honeycomb crystal lattice. If less this D/G ratio is than two

percent, then the CNTs of that spectrum are of high quality. It was found that the D/G ratio of the spectrum shown in Figure 4, (2500/67500) equals 3.7 percent. Therefore, it was deduced that the CNTs grown at this location are low quality CNTs. The G-band indicates the electrical properties of the CNTs. Its specific shape infers that these CNTs are semi-conducting.

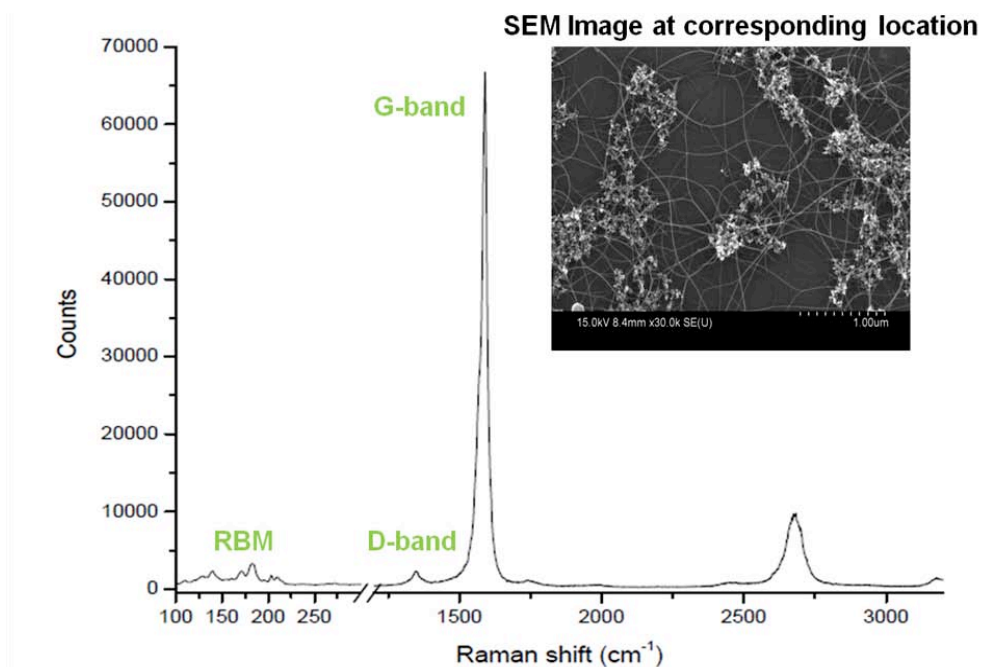


Figure 4. Raman Spectrum of H₂: 200 sccm sample, acquired at the center spot of the SEM image (inset).

4. Conclusion

Our results show that as H₂ flow rate increases from 100-300 sccm, the amount of CNTs increases to a peak density when H₂ flow rate is between 300-400 sccm.

However, the CNTs seem to grow less at higher H₂ flow rates such as 500 and 700 sccm.

5. Future Work

Studies are planned to continue to testing this thesis. Testing H₂ flow rates at smaller intervals between 300 and 400 sccm should result in a more defined optimum condition.

6. Acknowledgements

The authors would like to thank NSF-ERC grant number EEC-0812072, Dr. Brian Leroy, Jiamin Xue, UA Physics Dept., Lu Wang, Phil Anderson, and University Spectroscopy and Imaging Facilities (USIF) for their contributions towards this research project.

7. References

- [1] S. Ijima, "Helical microtubules of graphitic carbon," *Nature* 354, 56 (1991).
- [2] Y.C. Choi, W. Choi, *Carbon* 43 (2005), 2737-2741.
- [3] N. R. Franklin, Y. Li, R. J. Chen, A. Javey, H. Dai, *Applied Physics Letters*, Vol. 79, No. 27, (December 2001), 4571-4573.
- [4] W. Choi, D. Kim, Y. C. Choi, J. Haung, *Nanomaterials for Electronic Applications*, *JOM* (March 2007), 44-49.
- [5] B. Duong, Y. Peng, M. Ellis, S. Seraphin, H. Xin, "Combined Raman Spectroscopy and SEM Analysis of CVD Grown Carbon Nanotubes," *Proc. Microscopy and Microanalysis* (2008), 14:1130-1131CD.

[6] “Carbon Nanotubes & Buckyballs,” University of Wisconsin Madison
Material Research Science and Engineering Center, The Board of Regents of the
University of Wisconsin System, [2008].
<http://mrsec.wisc.edu/Edetc/nanoquest/carbon/index.html> [Accessed: 25 August
2010].

Low temperature thermodynamic properties of a polarized Fermi gas in a quartic trap

Mark DelloStritto and Theja N. De Silva

Department of Physics, Applied Physics and Astronomy,

The State University of New York at Binghamton, Binghamton, New York 13902, USA.

(Dated: August 25, 2010)

We study low temperature thermodynamic properties of a polarized Fermi gas trapped in a quartic anharmonic potential. We use a semi classical approximation and a low temperature series expansion method to derive analytical expressions for various thermodynamic quantities. These quantities include the total energy, particle number, and heat capacity for both positive and negative anharmonic confinements.

Keywords: anharmonic potential, chemical potential, Fermi-Dirac statistics, Fermi energy, fermions, polarized fermi gas, statistical mechanics, thermodynamics, Thomas-Fermi semi-classical approximation, specific heat

I. INTRODUCTION

Since its realization in dilute atomic gases, superfluidity of alkali atoms has been studied extensively in various externally controllable environments [1]. As a controllable parameter, the external trapping potential of a cold atomic system plays an important constrained role in current experimental setups. Most of the experiments are carried out in either magnetic or optical harmonic traps. A negative, but small quartic term is always present with the Gaussian optical potentials in current experimental setups. For the case of rapidly rotating Fermi gasses in harmonic traps, the force due to the trapping frequency almost balances the centrifugal force and the atomic cloud spreads in the plane perpendicular to the rotation axis. Therefore, an added positive quartic potential term ensures the stability of the fast rotating regime [2, 5]. Adding a positive quartic term is very important for a two-component superfluid Fermi system where the system is expected to be in the quantum Hall regime at the limit of extreme larger rotations [4].

Although the interaction between the atoms is extremely important in a system, the

problems are made tractable and the essential physics is retained by assuming fully polarized non-interacting atoms. Experimentally such a system can be prepared by trapping a single component (single hyperfine spin state) of atomic species. Because of the large spin relaxation time of the atoms compared to the other experimental time scales, single species can be retained over the entire time of the experiments. For a system of fully polarized Fermi gas, the s -wave scattering is prohibited due to the Pauli exclusion principle, while higher order partial wave scattering is negligible at low temperatures. Therefore, we model the system as a collection of non-interacting atoms obeying Fermi-Dirac statistics confined by quadratic and quartic potentials given as

$$\begin{aligned} V(r, z) &= \frac{1}{2}M\omega_r^2 r^2 + \frac{1}{2}M\omega_z^2 z^2 + \gamma r^4 \\ &= br^2 + b_z z^2 + \gamma r^4 \end{aligned} \tag{1}$$

where M is the atom mass, ω_i 's are the harmonic trapping frequencies ($i = r, z$), and $r^2 = x^2 + y^2$. Notice that we are using the cartesian coordinate system with coordinates (x, y, z) . We use Thomas-Fermi semiclassical approximation to derive various low temperature thermodynamic properties as a function of anharmonic confinement γ for *both* positive and negative values. Fast growing progress in the current experiments to manipulate quantum many body states in rotating Fermi gases motivated us to study the effect of positive γ values [5]. Experiments in harmonic traps are limited by the loss of confinement. This loss is due to centrifugal force when the rotation frequency approaches the axial harmonic trapping frequency. One can overcome this loss by adding a quartic term to the trap potential as already implemented in experiments [5]¹. On the other hand, the small negative quartic term present with the Gaussian optical potential can be canceled by adding an extra quartic term. We will show later, that the minimum negative γ value at which the atomic cloud is confined depends on the total number of atoms present in the system. Thermodynamic properties of Fermi gases confined in a harmonic trap have been studied in Ref. [6]. In a recent work, interplay between rotation and anharmonicity of a Fermi gas has been studied extensively in Ref. [7]. In the superfluid phase of a two-component gas, the effect of anharmonicities on breathing mode frequencies in the Bardeen-Cooper-Schrieffer- BEC crossover

¹ We do not consider rotation in the present work. Fast rotating Fermi gas can be linked to one of the very interesting phenomena; integer quantum Hall effect.

regime has been presented in Ref. [8]. Thermodynamic properties of a Bose gas confined in a quartic potential trap can be found in ref. [9].

This paper is organized as follows. In section II, we present the derivation of thermodynamic quantities within our framework of semiclassical approximation. In section III, we present our results discussing how these thermodynamic quantities depend on trap potential parameters. Finally in section IV, we draw our conclusions.

II. FORMALISM

We consider a polarized Fermi atomic system trapped in an external potential which has both harmonic and radial quartic components given in Eq. 1. For the atoms at thermal equilibrium, the average number of atoms in the single particle state $|\alpha\rangle$ with energy ϵ_α is given

$$n_\alpha = \frac{1}{e^{\beta(\epsilon_\alpha - \mu)} + 1} \quad (2)$$

where μ is the chemical potential and $\beta = 1/(k_B T)$, with k_B the Boltzmann constant and T the temperature. The average number $N = \sum_\alpha g n_\alpha$ of atoms of the system fixes the chemical potential. The total energy $U = \sum_\alpha g \epsilon_\alpha n_\alpha$, where the spin degenerate factor $g = 1$ because the fermions are polarized. When the number of atoms in the system is large and the average potential energy of atoms in the trap is much smaller than the kinetic energy of the atoms, Thomas-Fermi semiclassical approximation can be used. The semiclassical approximation means that, instead of ϵ_α , we can use the classical single-particle phase space energy $\epsilon(r, p) = p^2/(2M) + V(r, z)$. In general, at high enough temperatures, the particles are classical so that the semiclassical approximation is valid. In the present paper, we are considering a spin polarized Fermi system. As a result of the Pauli exclusion principle, when the temperature goes to zero, Fermi atoms fill every energy level up to the Fermi energy E_F (the energy of the highest occupied state). If the system has large number of atoms, then the Fermi energy E_F of the system is larger than the single atom ground state energy². Therefore, a spin-polarized Fermi gas can be well described in the semiclassical

² For a system with large enough atom numbers, majority of atoms will have average energy in the order of E_F .

approximation even at very low temperatures. This is drastically different for bosons where thermal energy $k_B T$ has to be compared with the ground state energy.

Using the quantum elementary volume of the single-particle phase space, h^3 , where h is the Plank constant, the total number of atoms and the energy of the system have the forms

$$N = \frac{g}{h^3} \int \frac{d^3 r d^3 p}{Z^{-1} e^{\beta \epsilon(r,p)} + 1} \quad (3)$$

and

$$U = \frac{g}{h^3} \int \frac{\epsilon(r,p) d^3 r d^3 p}{Z^{-1} e^{\beta \epsilon(r,p)} + 1}. \quad (4)$$

Here $Z = e^{\beta \mu}$. Writing the volume of the momentum element $d^3 p = 4\pi p^2 dp$ and changing of variables $\beta p^2 / (2M) \rightarrow x$, these two equations can be written in the forms,

$$N = \frac{g}{h^3} \left(\frac{2M\pi}{\beta} \right)^{3/2} \int d^3 r f_{3/2}(z_r) \quad (5)$$

and

$$U = \frac{3g}{2h^3} (2M\pi)^{3/2} \frac{1}{\beta^{5/2}} \int d^3 r f_{5/2}(z_r) + \frac{g}{h^3} \left(\frac{2M\pi}{\beta} \right)^{3/2} \int d^3 r V(r, z) f_{3/2}(z_r). \quad (6)$$

Here $z_r^{-1} = Z^{-1} e^{\beta V(r,z)}$, and the Fermi integral $f_l(z_r)$ is given by

$$f_l(z_r) = \frac{1}{\Gamma(l)} \int_0^\infty \frac{x^{l-1} dx}{z_r^{-1} e^x + 1} \quad (7)$$

where $\Gamma(l) = \int_0^\infty t^{l-1} e^{-t} dt$ is the Gamma function. For low temperatures (or large z_r values), we expand $f_l(z_r)$ as an asymptotic series—commonly known as Sommerfeld's lemma [10],

$$f_l(z_r) = \frac{\ln z_r}{\Gamma(l+1)} \left[1 + l(l-1) \frac{\pi^2}{6} \frac{1}{(\ln z_r)^2} + l(l-1)(l-2)(l-3) \frac{7\pi^2}{360} \frac{1}{(\ln z_r)^4} + \dots \right]. \quad (8)$$

Writing the volume element $\int d^3 r = 2 \int_0^{z_0} dz \int_0^{r_\perp(z)} 2\pi r_\perp dr_\perp$, with the edges³ of the atomic cloud $r_\perp^2(z) = \sqrt{b^2/(4\gamma^2) + (\mu - b_z z^2)/\gamma} - b/(2\gamma)$ and $z_0 = \sqrt{\mu/b_z}$ [note b and b_z are defined

³ Effective chemical potential $\mu - V(r, z)$ monotonically decreases from center to the edge of the trap. So that the edge of the trap is determined by the condition $\mu - V(r, z) = 0$.

in Eq (1)], we can perform the spatial integration to obtain analytical expressions for the number of atoms and the total energy;

$$N = \frac{g\lambda}{\sqrt{\pi|\tilde{\gamma}|}} \left[\frac{4}{3\pi} \tilde{\mu}^{5/2} I_{N1}(A) + \frac{\pi^{3/2}}{6} \tilde{\mu}^{1/2} \tilde{T}^2 I_{N2}(A) + \mathcal{O}(\tilde{T}^3) \right] \quad (9)$$

and

$$\tilde{E} = \frac{g\lambda}{\sqrt{|\tilde{\gamma}|}} \tilde{\mu}^{7/2} I_{E1}(A) + \frac{g\pi\lambda}{\sqrt{|\tilde{\gamma}|}} \tilde{\mu}^{3/2} \tilde{T}^2 I_{E2}(A) + \mathcal{O}(\tilde{T}^3) \quad (10)$$

where we have defined the dimensionless variables $\tilde{E} \equiv U/(\hbar\omega_r)$, aspect ratio⁴ of the harmonic trap $\lambda \equiv \omega_r/\omega_z$, $\tilde{\gamma} \equiv \hbar\gamma/(M^2\omega_r^3)$, $\tilde{\mu} \equiv \mu/(\hbar\omega_r)$, $\tilde{T} \equiv k_B T/(\hbar\omega_r)$, and $A \equiv (1/16)[1/(|\tilde{\gamma}|\tilde{\mu})]$. The dimensionless functions $I_{N1}(x)$, $I_{N2}(x)$, $I_{E1}(x) = 4I_{U1}(x)/5 + 4[I_{U3}(x) + I_{U4}(x)]/3$, and $I_{E2}(x) = I_{U2}(x)/2 + [I_{U5}(x) + I_{U6}(x)]/6$ are defined below. The upper sign is for positive values of γ while the lower sign is for negative values of γ .

$$I_{N1}(x) = \frac{1}{80} \left(\pm 8(\pm 1 + x)^{5/2} \pi \mp \sqrt{x}(15 \pm 20x + 8x^2)\pi \right) \quad (11)$$

$$I_{N2}(x) = \pm \frac{\sqrt{x}\pi}{2} \pm \frac{\sqrt{\pm 1 + x}\pi}{2} \quad (12)$$

$$I_{U1}(x) = \frac{1}{96} \left(\mp \frac{15}{16} \sqrt{x}\pi (8x^2 \pm 16x + 11) \mp \frac{3}{112} \sqrt{x} (\pm 256x^3 + 616x^2 \pm 560x + 175) \pi \right. \\ \left. + \frac{48 (x^{9/2} \pm 4x^{7/2} + 6x^{5/2} \pm 4x^{3/2} + \sqrt{x}) \pi}{7\sqrt{x}\sqrt{x \pm 1}} \right) \quad (13)$$

$$I_{U2}(x) = \frac{1}{4} \left(\frac{2(x^{5/2} \pm 2x^{3/2} + \sqrt{x})\pi}{3\sqrt{x}\sqrt{x \pm 1}} - \frac{1}{3} \sqrt{x}(2x \pm 3)\pi \right) \quad (14)$$

$$I_{U3}(x) = \frac{1}{280} \left(24x^{7/2} - 24\sqrt{x \pm 1}x^3 \pm 56x^{5/2} \mp 44\sqrt{x \pm 1}x^2 + 35x^{3/2} \right. \\ \left. - 16\sqrt{x \pm 1}x \pm 4\sqrt{x \pm 1} \right) \pi \quad (15)$$

⁴ The aspect ratio of a thermal cloud is the ratio of the radial to axial size in a harmonic potential.

$$I_{U4}(x) = \frac{1}{560} \left(8(x \pm 1)^{7/2} \pi - \frac{1}{2} \sqrt{x} (16x^3 \pm 56x^2 + 70x \pm 35) \pi \right) \quad (16)$$

$$I_{U5}(x) = \frac{(-2x^2 + 2\sqrt{x \pm 1}x^{3/2} \mp x + 1) \pi}{6\sqrt{x \pm 1}} \quad (17)$$

$$I_{U6}(x) = \frac{2 \mp 3\sqrt{x(x \pm 1)} \pm 4x - 2\sqrt{x \pm 1}x^{3/2} + 2x^2}{12\sqrt{x \pm 1}}. \quad (18)$$

The recurring \pm sign originates from the sign of γ in the integrals. Finally, we derive heat capacity $C = (\partial U / \partial T)|_N$ of the system using Eq. (10). First, we write

$$\begin{aligned} \frac{\partial U}{\partial T} \Big|_N &= \frac{k_B}{\hbar \omega_r} \frac{\partial U}{\partial \tilde{T}} \Big|_N \\ &= \frac{dU}{d\tilde{T}} + \frac{\partial U}{\partial \tilde{\mu}} \frac{\partial \tilde{\mu}}{\partial \tilde{T}}. \end{aligned} \quad (19)$$

As the number of atoms in the trap is fixed, using the condition $\partial N / \partial \tilde{\mu} = 0$, we find $\partial \tilde{\mu} / \partial \tilde{T}$ to obtain the heat capacity,

$$\frac{C}{k_B} = \frac{2g\pi\lambda\tilde{\mu}^{3/2}}{\sqrt{|\tilde{\gamma}|}} \tilde{T} I_{E2}(A) - \frac{\pi^2 \tilde{T}}{10 \tilde{\mu}} \left(\frac{7g\lambda\tilde{\mu}^{5/2}}{2\pi\sqrt{|\tilde{\gamma}|}} I_{E1}(A) - \frac{g\lambda\tilde{\mu}^{3/2}}{16\pi|\tilde{\gamma}|^{3/2}} \frac{\partial I_{E1}(A)}{\partial A} \right) \frac{I_{N2}(A)}{I_{N1}(A)} + \mathcal{O}(\tilde{T}^3) \quad (20)$$

III. RESULTS

In this section we present thermodynamical properties as a function of temperature and trap potential parameters. For our calculations, we use a large number of atoms (1.0×10^4) to ensure the validity of our semi-classical treatment. First we solve Eq. 5 for $\tilde{\mu}$ for given N , T , and λ . As can be seen from FIG. 1, while the chemical potential increases with the anharmonic term, it decreases as the aspect ratio(λ) increases. As more energy is needed to excite the fermions in low aspect ratio traps, the chemical potential in low aspect ratio traps is larger than that of higher aspect ratio traps. As we are using large number of atoms for our calculations, anharmonic term cannot be too negative. If the anharmonic term is too negative relative to the harmonic confinement, the trapped atoms cannot be confined as the

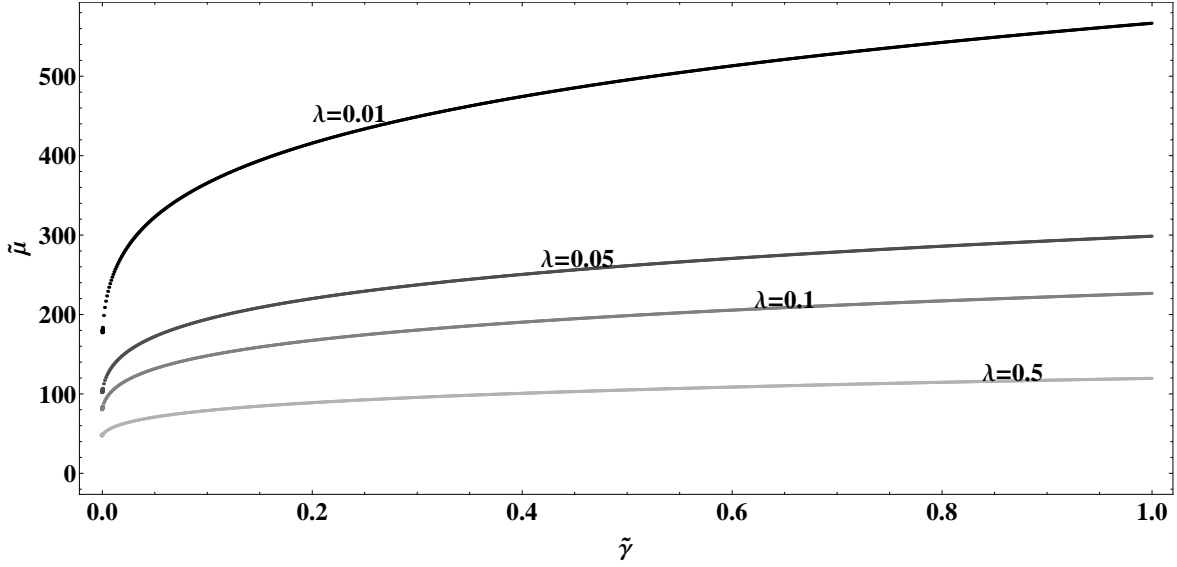


FIG. 1: Chemical potential as a function of anharmonic term γ for fixed number of atoms $N = 1.0 \times 10^4$. We fixed the temperature to be $k_B T = \hbar \omega_r$. Different lines represent different aspect ratios λ .

potential is not bounded from below. The value of the anharmonicity at the point where it dominates over the harmonic confinement will be called critical anharmonicity hereafter. This critical anharmonicity depends on the number of atoms in the trap. For a set of representative parameters, this critical anharmonic value as a function of atom number is given in FIG. 2. Chemical potential for a range of negative anharmonic potential is given in FIG. 3.

In FIG. 4, we plot the total energy as a function of anharmonic term. For given values of atomic number N , temperature T , and aspect ratio λ , we first calculate the chemical potential from Eq. 9, and then we use this chemical potential to calculate the energy from Eq. 10. As can be seen in FIG. 4, for fixed number of atoms and fixed aspect ratio λ , dimensionless energy increases as we increase the anharmonic term γ . This is because of the trapping potential energy increases with increasing γ .

The low temperature behavior of the heat capacity calculated from Eq. (20) is shown in FIGS. 5-7. The temperature dependence of the heat capacity for different values of γ and λ is shown in FIG. 5 and FIG. 6. As we have considered up to the linear order in temperature, the specific heat is linear with temperature, however, the slope change significantly as we change the values of γ or λ . The heat capacity of the polarized Fermi gas increases monotonically as

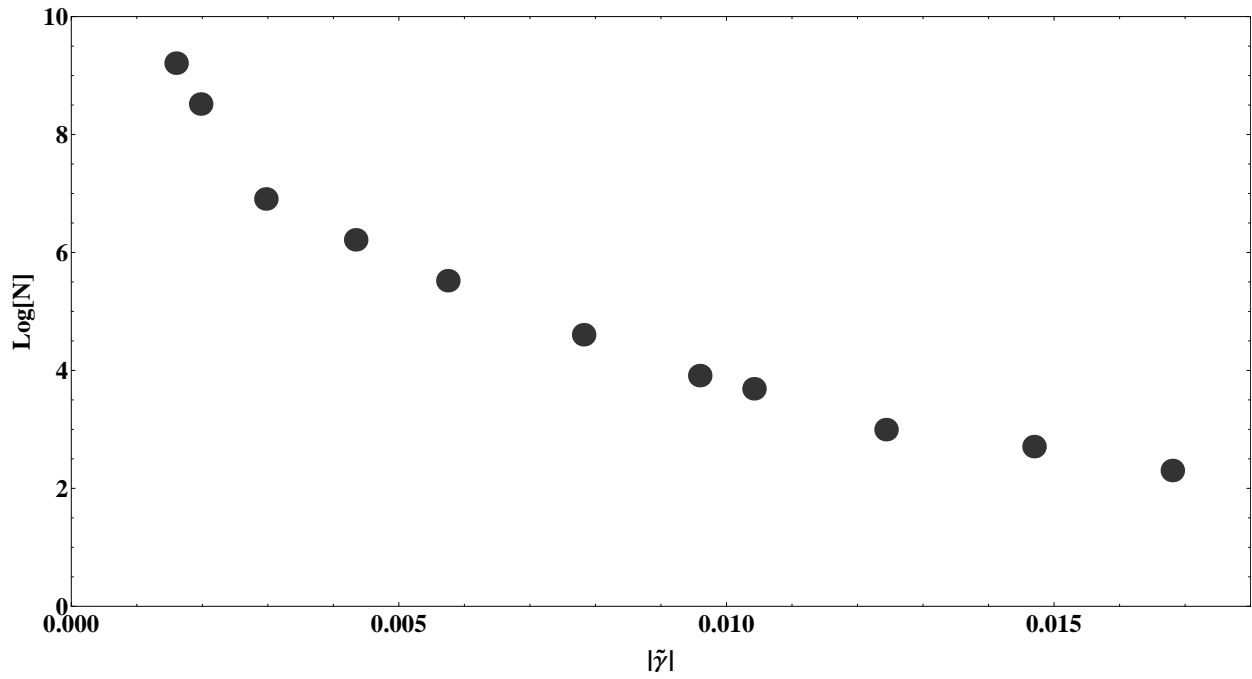


FIG. 2: The critical negative anharmonic dependence on number of atoms in the trap for $k_B T = \hbar \omega_r$ and $\lambda = 1$. The atomic cloud is unstable below this critical value.

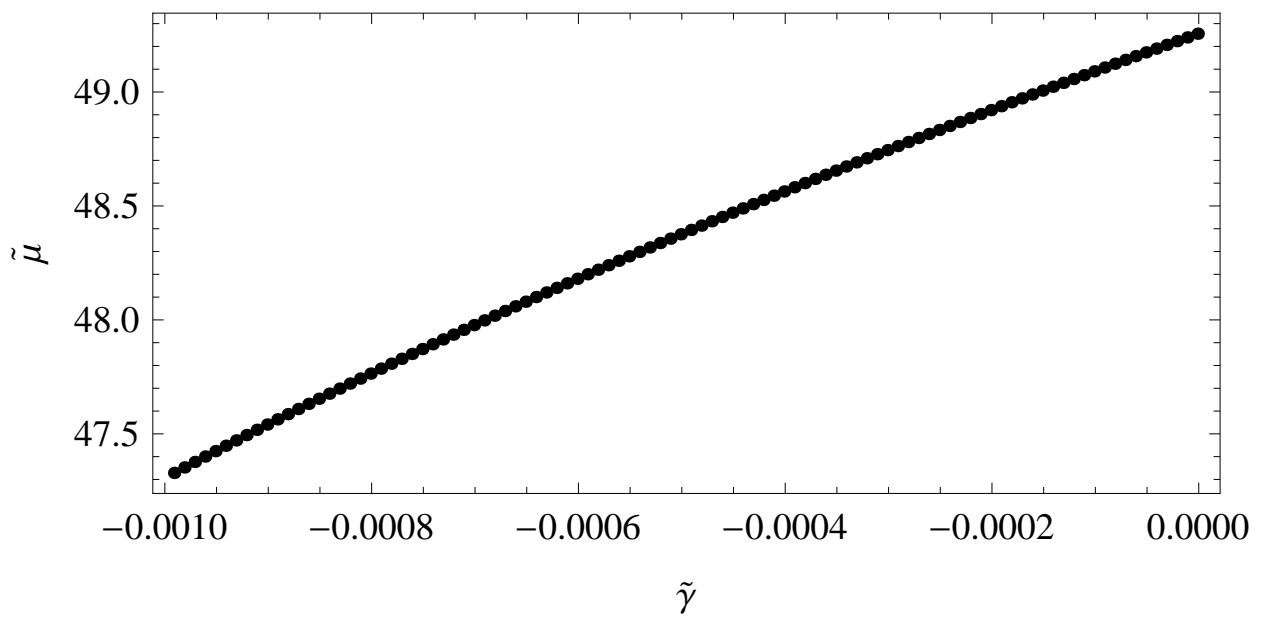


FIG. 3: Chemical potential for negative anharmonic potentials. We fixed the temperature, number of atoms, and aspect ratio to be $k_B T = \hbar \omega_r$, $N = 1.0 \times 10^4$, and $\lambda = 0.5$. For $\tilde{\gamma} < -0.001$, the system is unstable.

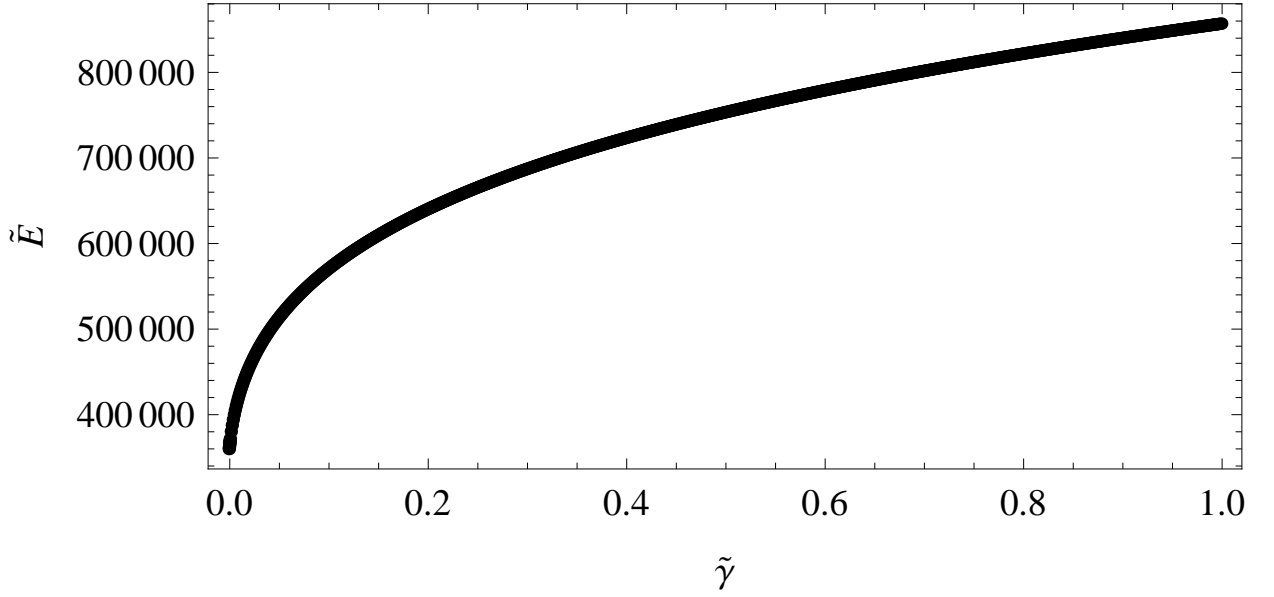


FIG. 4: Total energy as function of anharmonic term γ for fixed number of atoms $N = 1.0 \times 10^4$. We fixed the temperature to be $k_B T = \hbar \omega_r$ and the aspect ratio $\lambda = 0.5$. For these selected parameters, absolute value of critical $|\gamma|$ is 0.001.

the temperature increases. This behavior is completely different from a Bose gas [11] where the heat capacity shows a maximum at superfluid-normal phase transition point. As can be seen from the figures, the heat capacity decreases with increasing anharmonic term γ . This decrease is due to the confinement effects which can be clearly seen from Eq. 20.

IV. CONCLUSIONS

We have considered a spin-polarized Fermi gas trapped in an anharmonic potential. Applying a semiclassical treatment to the particle number and energy, and using a low-temperature series expansion method, we have derived analytical expressions for several thermodynamic quantities. We have discussed the trap parameter dependence on these quantities and the results were presented as a function of anharmonic trap parameter and temperature. The results of our paper can be tested in a lab by a similar experimental procedure carried out by Bretin *et al.* [5] for Bose-Einstein condensates in a quartic trap.

In the present work, we considered fully polarized fermions. At low temperatures and low densities, s -wave short-range interactions are prohibited and higher wave scattering are strongly suppressed. The most natural extension of this work would be the inclusion of

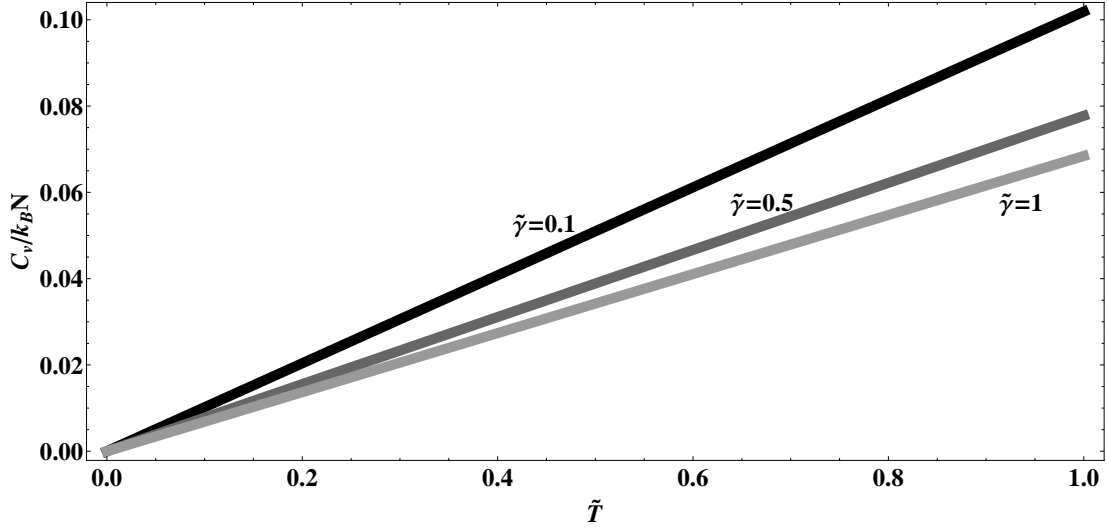


FIG. 5: Specific heat as function of temperature for fixed number of atoms $N = 1.0 \times 10^4$. We fixed the aspect ratio to be $\lambda = 0.5$.

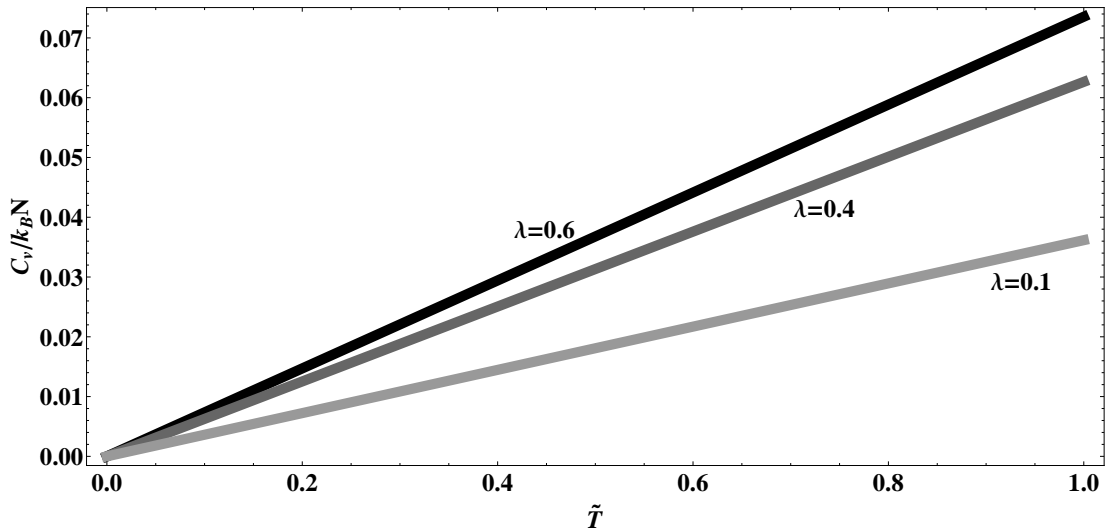


FIG. 6: Specific heat as function of temperature for fixed number of atoms $N = 1.0 \times 10^4$ and $\tilde{\gamma} = 0.5$.

interaction. This can be done by adding another Zeeman state of atoms and consider the system as a two component fermions. A particular interesting regime is so called unitarity regime, where the scattering length between atoms is infinite. This regime is located near the Feshbach resonance [12]. At this point, the interaction parameter disappears from the physical quantities. Therefore, all thermodynamic quantities are universal function of the

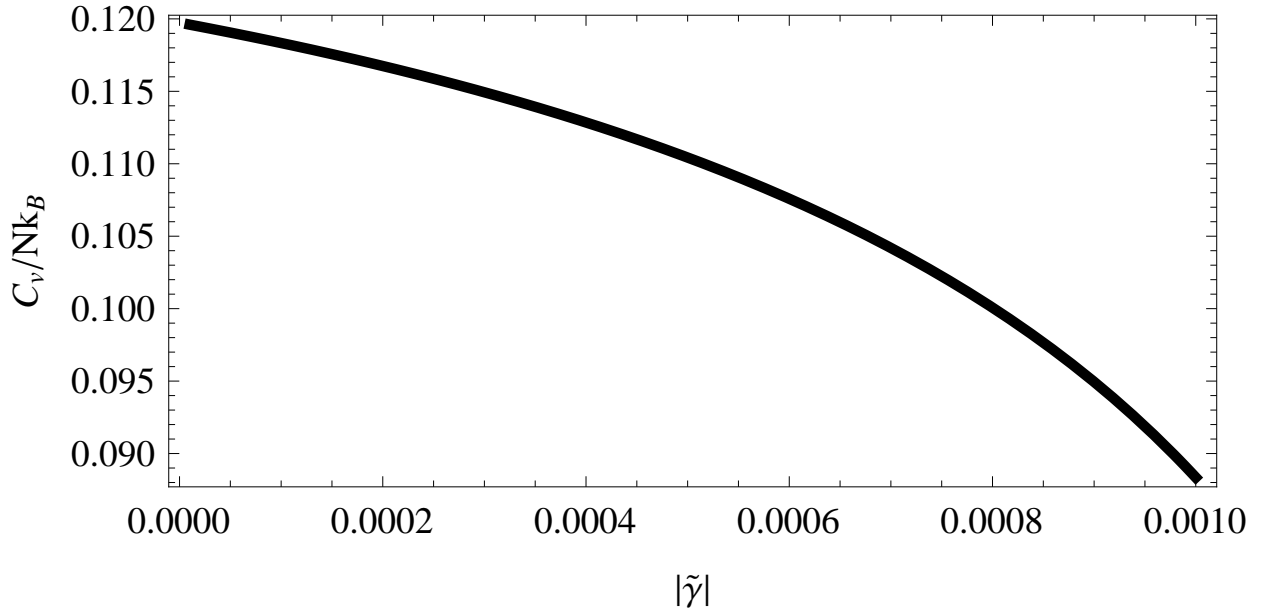


FIG. 7: Specific heat as function of γ for negative γ 's. We fixed the number of atoms $N = 1 \times 10^4$. We fixed the $k_B T = \hbar \omega_r$.

dimensionless temperature $k_B T / \epsilon_F$, where ϵ_F is the Fermi energy [13]. However, as there is no small parameter, it is difficult to reliably calculate thermodynamic quantities close to the unitarity regime. Therefore, one has to rely on good experimental data of energy, heat capacity, etc. [14]. Then by comparing experimental data at unitarity regime with non-interacting calculation of thermodynamic quantities allows one to find the scaling factors. An accurate determination of these scaling factors of unitary Fermi gases is one of the challenging and fascinating theoretical problems at the moment [15].

-
- [1] M. H. Anderson, J. R. Ensher, M. R. Matthews, C. E. Wieman, E. A. Cornell, *Science* **269**, 198-201, (1995); K.B. Davis, M.-O. Mewes, M.R. Andrews, N.J. van Druten, D.S. Durfee, D.M. Kurn, and W. Ketterle, *Phys. Rev. Lett.* **75**, 3969, (1995); C. C. Bradley, C. A. Sackett, J. J. Tollett, and R. G. Hulet, *Phys. Rev. Lett.* **75**, 1687 (1995); B. DeMarco, D. S. Jin, *Science* **285**, 1703-1706 (1999); A. G. Truscott, K. E. Strecker, W. I. McAlexander, G. B. Partridge, R. G. Hulet, *Science* **291**, 2570-2572 (2001); K. M. O'Hara, S. L. Hemmer, M. E. Gehm, S. R. Granade, J. E. Thomas, *Science* **298**, 2179-2182, (2002); C. A. Regal, M. Greiner, and D. S. Jin, *Phys. Rev. Lett.* **92**, 040403 (2004); M. W. Zwierlein, C. A. Stan, C. H. Schunck, S. M. F.

- Raupach, A. J. Kerman, and W. Ketterle, *Phys. Rev. Lett.* **92**, 120403 (2004); C. Chin et al., *Science* **305**, 1128-1130 (2004); T. Bourdel, L. Khaykovich, J. Cubizolles, J. Zhang, F. Chevy, M. Teichmann, L. Tarruell, S. J. J. M. F. Kokkelmans, and C. Salomon, *Phys. Rev. Lett.* **93**, 050401 (2004); J. Kinast, S. L. Hemmer, M. E. Gehm, A. Turlapov, and J. E. Thomas, *Phys. Rev. Lett.* **92**, 150402 (2004); J. J. Kinast, S. L. Hemmer, M. E. Gehm, A. Turlapov, and J. E. Thomas, *Phys. Rev. Lett.* **92**, 150402 (2004); M. Bartenstein, A. Altmeyer, S. Riedl, S. Jochim, C. Chin, J. H. Denschlag, R. Grimm, *Phys. Rev. Lett.* **92**, 203201 (2004).
- [2] A. L. Fetter, *Phys. Rev. A* **64**, 063608 (2001).
- [3] V. Bretin, S. Stock, Y. Seurin, and J. Dalibard, *Phys. Rev. Lett.* **92**, 050403 (2004).
- [4] H. Zhai and T. -L. Ho, *Phys. Rev. Lett.* **97**, 180414 (2006); M. Y. Veillette, D. E. Sheehy, L. Radzihovsky, and V. Gurarie, *Phys. Rev. Lett.* **97**, 250401 (2006); G. Moller and N. R. Cooper, *Phys. Rev. Lett.* **99**, 190409 (2007); N. R. Cooper, N. K. Wilkin, and J. M. Gunn, *Phys. Rev. Lett.* **87**, 120405 (2001); B. Paredes, P. Zoller, and J. I. Cirac, *Sol. S. Com.* **127**, 155 (2003).
- [5] V. Bretin, S. Stock, Y. Seurin, J. Dalibard, *Phys. Rev. Lett.* **92**, 050403 (2004)
- [6] G. M. Bruun and K. Burnett, *Phys. Rev. A* **58** (1998); E. J. Mueller, *Phys. Rev. Lett.* **93**, 190404 (2004); X. X. Yi and J. C. Su, *Physica Scripta*, **60**, 117 (1999); L. Salasnich, B. Pozzi, A. Parola, and L. Reatto, *J. Phys. B: At. Mol. Opt. Phys.* **33**, 3943 (2000).
- [7] K. Howe, A. R. P. Lima, and A. Pelster, *Eur. Phys. J. D* **54** (2009).
- [8] T. N. De Silva. *Phys. Rev. A* **78**, 023623 (2008).
- [9] E. Lundh, *Phys. Rev. A* **65**, 043604 (2002); K. Kasamatsu, M. Tsubota, and M. Ueda, *Phys. Rev. A* **66**, 053606 (2002); G. Kavoulakis and G. Baym, *New J. Phys.* **5**, 51 (2003); E. Lundh, A. Collin, and K. A. Suominen, *Phys. Rev. Lett.* **92**, 070401 (2004); T. K. Ghosh, *Phys. Rev. A* **69**, 043606 (2004); T. K. Ghosh, *Eur. Phys. J. D* **31**, 101 (2004); G. M. Kavoulakis, A. D. Jackson, and Gordon Baym, *Phys. Rev. A* **70**, 043603 (2004); I. Danaila, *Phys. Rev. A* **72**, 013605 (2005); A. Collin, *Phys. Rev. A* **73**, 013611 (2006); S. Bargi, G. M. Kavoulakis, and S. M. Reimann, *Phys. Rev. A* **73**, 033613 (2006); Michiel Snoek and H. T. Stoof, *Phys. Rev. A* **74**, 033615 (2006); S. Gautam, D. Angom, *Eur. Phys. J. D* **46**, 151155 (2008).
- [10] R.K. Pathria, *Statistical Mechanics*, 2nd ed., Page 510 (Butterworth-Heinemann, 1996).
- [11] S. Kling and A. Pelster, *Phys. Rev. A* **76**, 023609 (2007).
- [12] U. Fano, *Phys. Rev.* **124**, 1866 (1961); H. Feshbach, *Ann. Phys.* **5**, 357 (1958).

- [13] T. -L. Ho, *Phys. Rev. Lett.* **92**, 090402 (2004).
- [14] J. Kinast, A. Turlapov, J. E. Thomas, Q. Chen² J. Stajic, and K. Levin, *Science*, **307**, 1296-1299 (2005).
- [15] J. Carlson *et al.*, *Phys. Rev. Lett.* **91**, 050401 (2003); S. Y. Chang *et al.*, *Phys. Rev. A* **70**, 043602 (2004); J. Carlson and S. Reddy, *Phys. Rev. Lett.* **95**, 060401 (2005); G. E. Astrakharchik *et al.*, *Phys. Rev. Lett.* **93**, 200404 (2004); A. Bulgac, J. E. Drut, and P. Magierski, *Phys. Rev. Lett.* **96**, 090404 (2006); A. Bulgac, J. E. Drut, and P. Magierski *Phys. Rev. Lett.* **99**, 120401 (2007).

A New Assessment of Dark Matter in the Milky Way Galaxy

Grant Remmen

August 19, 2010

School of Physics and Astronomy, 116 Church Street S.E.,
College of Science and Engineering, University of Minnesota, Minneapolis, MN, United States
Address for correspondence: 272 Cherry Ridge Drive, Detroit Lakes, MN
E-mail address: remme024@umn.edu

Abstract

Through an examination of recent data on the mass distribution and velocity curve of the Milky Way Galaxy, I produce a new estimate of the dark matter distribution, as well as the overall dark matter content, of our galaxy. Initially, I develop a model of the baryonic mass of the galaxy (i.e. luminous matter and interstellar clouds). This model incorporates three components: an exponential stellar disc and a central stellar bulge, based on the Tuorla–Heidelberg model, and a gaseous layer, fit to the gas density distribution data of Olling & Merrifield (2001). Secondly, incorporating recent data, I calculate an updated rotational velocity curve for the galaxy as a function of galactocentric radius. Using this velocity curve, I determine total galactic mass as a function of radius and compare this with the baryonic mass model to determine the distribution of dark matter in the galaxy, with improved precision and over a greater spatial range than previous estimates. This calculation results in a radial dark matter density distribution that falls off with large distance in a characteristic fashion. Finally, I show that neutrinos, particles that have often been suggested as a component of dark matter, cannot make up more than a very small amount of the galactic dark matter content.

Key Words : Galaxy: kinematics and dynamics, Galaxy: structure, dark matter, neutrinos

1 Introduction

For many years, it has been known that the observed rotation rates of spiral galaxies differ greatly from the rates predicted based on the observable luminous masses of the galaxies. This simple observation has led to the proposition that large amounts of invisible matter, known as dark matter, are distributed within and around these galaxies, accounting for the greater gravity and thus faster rotation than what would be predicted from the luminous mass alone. While this is accepted as fact and the dark matter distribution associated with various cosmic objects has been determined, a point of constant curiosity has been the dark matter distribution within our home galaxy. The following determination of the pattern and content of the dark matter halo within the Milky Way will allow for more decisive and conclusive experimentation in the future, through the detection of particles, such as neutrinos, that have been proposed as candidates to explain the effects of dark matter. Further, the dark matter distribution of the galaxy is of great theoretical interest with regard to the dynamics of our galaxy as it formed and evolved.

In calculating the distribution of the Milky Way’s dark matter halo, I assume that the Gaussian approximation for gravity is applicable to the galaxy. Specifically, this means that, for a piece of matter located at a given galactocentric radius, the net gravitational force at that position is equal to the gravitational force due to the mass interior to that radius and acts as though this entire interior mass were concentrated at the center of the galaxy. This approximation is mathematically valid and exact for any spherically symmetric mass distribution, by Gauss’ law for gravity, or alternatively by Newton’s law of universal gravitation. However, the Gaussian approximation is a commonly used tool in studies of galactic rotation. As shown by Binney & Tremaine (1987), the peak rotational velocity within an exponential disc as compared to the peak velocity within the corresponding spherically distributed body is higher only by approximately 15 percent, while the velocities at large radii differ by only a negligible amount. Furthermore, the galaxy has more of a spherical character than that of a pure exponential disc, as a result of its central stellar bulge. Thus, while the assumption of the applicability of Gauss’ law for gravity in this manner may cause the supposition of a bit more dark matter within the interior of the galaxy, the calculation of the total amount of dark matter interior to large radii will not be adversely affected by this method.

Once the supposition of the Gaussian approximation for gravity has been accepted, the calculation of the mass interior to a galactocentric radius, given the circular velocity of matter at that radius, is straightforward. By equating the magnitude of the centripetal acceleration to the gravitational force per unit mass, one may deduce that:

$$M_V(R) = \frac{R[V(R)]^2}{G}, \quad (1)$$

where $M_V(R)$ denotes the total mass (based on the velocity curve) interior to a galactocentric radius R .

In all calculations, I use the latest (2006) value of $G = 6.67428 \times 10^{-11} \text{ m}^3 \text{ kg}^{-1} \text{ s}^{-2}$, specified by the Committee on Data for Science and Technology (CODATA) of the International Council for Science and accepted by the National Institute of Standards and Technology (NIST) (Mohr, Taylor & Newell 2007). For an accurate definition of the kiloparsec in units of meters, I use the value from the Explanatory Supplement to the Astronomical Almanac (Seidelmann 2005): $1 \text{ kpc} = 3.085677582 \times 10^{19} \text{ m}$. Finally, for the unit of the solar mass, I use the official value provided by the National Aeronautics and Space Administration (NASA) of $1.989100 \times 10^{30} \text{ kg}$ (Williams 2004).

First, however, in Section 2, I shall describe a model for the baryonic mass distribution of the galaxy. This mass model consists of a density function $\rho_{\text{model}}(R)$, which is assumed to be a function of radius only. That is, consistent with the above discussion, the mass of the galaxy is considered to have the form of the equivalent spherically symmetric mass distribution, for the purposes of the Gaussian approximation for the gravitational pull of matter interior to a given galactocentric radius. As will be shown in the following Section, the baryonic mass model for the galaxy has the form

$$\rho_{\text{model}}(R) = \begin{cases} \frac{1}{2R} \Sigma_0 e^{-R/R_d} & \text{disc} \\ \frac{\rho_{\text{bulge},0}}{\eta \zeta b_m^3} \frac{\exp[-(R/b_m)^2]}{(1+R/b_0)^{1.8}} & \text{bulge} \\ \sum_{i=1}^3 \frac{G_i}{2} R^{i-1} \text{ for } R \leq 23.521 \text{ kpc} & \text{interstellar gas} \end{cases}, \quad (2)$$

where the constants for each component are defined in their respective portion of Section 2 (Section 2.1 for the disc, 2.2 for the bulge, and 2.3 for the interstellar gas). As will be demonstrated in Section 2, to find the total baryonic mass interior to a given galactocentric radius, the density function is integrated: $M_{\text{model}}(R) = 4\pi \int_0^R r^2 \rho_{\text{model}}(r) dr$.

In all final results of calculations (both in text and in Table 5), values are rounded to an appropriate number of significant figures. However, the reader should note that, consistent with previous studies of the velocity curve (e.g. Clemens 1985), I report values of the constants for the curve to a large number of figures to preserve continuity of the curve and reproducibility of the calculation. Since the

velocity curve is a piecewise function, rounding leads to gaps in the curve; these gaps would create difficulties for an interested reader reproducing the calculation or using the model for other purposes. Though the models are robust, it is useful to preserve more digits in intermediate results, so as not to introduce roundoff errors in subsequent calculations. For these reasons, I report the constants for all intermediate calculational steps (velocity curve, baryonic mass model, etc.) to a large number of figures, as in Tables 1 through 4 and Equation 15. Nonetheless, all final quoted results are rounded to significant figures.

2 The Mass Model of the Milky Way Galaxy

The “normal” matter of the Milky Way Galaxy, also known as the baryonic mass, is composed primarily of three components: an exponential disc of stars that thins out dramatically at large distances from the galactic center, a central stellar bulge, and a distribution of atomic and molecular gas consisting primarily H I and H₂ (neutral atomic and molecular hydrogen, respectively). For the exponential disc and central bulge, I employ the results of the Tuorla–Heidelberg study (Flynn et al. 2006), as adapted by McGaugh (2008). The Tuorla–Heidelberg study encompasses a detailed measurement and modeling of the mass-to-light ratio for the Milky Way, resulting in a surface density function of the galactic disc. Using the Tuorla–Heidelberg surface density model, I develop a volumetric density model and a total disc mass model as a function of galactocentric radius. The surface density of the disc is defined as the mass per square kiloparsec of galactic disc stars, treating the galaxy as a flat plate of variable density (the Tuorla–Heidelberg “flat plate” method is standard among studies of the galactic mass distribution). That is, the surface density, in effect, is the integral of the (true) volumetric mass density of the galaxy over the thickness of the disc, yielding a figure with units of mass per unit area. McGaugh makes use of the Tuorla–Heidelberg and other results to develop a detailed mathematical model of the galaxy’s disc and bulge density distributions, then employs these models in an application of the theory of modified Newtonian dynamics (MOND) to the galaxy. MOND is an alternative to the dark matter explanation for the apparent “missing mass” of galaxies. McGaugh’s presentation of the Tuorla–Heidelberg study results in a disc and bulge mass model of the galaxy that is consistent with known data regarding the surface density of the disc at the solar radius (i.e. the radius of our solar system’s orbit about the galactic center), as well as the overall (global) luminosity of the galaxy. Thus, the disc may be assumed to be essentially flat in the surface density equation. To the Tuorla–Heidelberg model, I add the distribution of interstellar gas; based on the data from the study by Olling & Merrifield (2001), I derive a density function for the atomic and molecular hydrogen distribution. Note: for all of the equations given in this Section, masses are expressed in units of solar masses (M_{\odot}), while all distances are in units of kiloparsecs (kpc).

2.1 The Milky Way’s exponential stellar disc

Consistent with McGaugh (2008), I adopt a stellar disc distribution as a function of galactocentric radius R according to the following formula:

$$\Sigma_{\text{disc}}(R) = \Sigma_0 e^{-R/R_d}, \quad (3)$$

where R_d denotes the scale length, a value of a galactocentric radius by which to scale this exponential function. In order to be consistent with accurate and up-to-date experimental data, I have used a value of 2.5 kpc for R_d , consistent with the L -band data from the *COBE* satellite (Binney, Gerhard & Spergel 1997). The L -band is an infrared window: a narrow range of infrared radiation at approximately 3.5 μm for which Earth’s atmosphere is fairly transparent. Further, for consistency with the Tuorla–Heidelberg model (Flynn et al. 2006), I use a value for Σ_0 of 960 $M_{\odot} \text{pc}^{-2}$ from table 1 in McGaugh (2008), equivalent to $9.60 \times 10^8 M_{\odot} \text{kpc}^{-2}$.

From Equation 3, I compute two other formulae for use in calculations. First, I convert the function for the surface density of the disc to a three-dimensional volumetric density as a function of radius. In

effect, the galaxy will no longer be treated as a flat plane of stars, but will be assumed for calculational purposes to be a spherically symmetric body. This normalization is accomplished by the following procedure, which may be visualized geometrically. The differential mass contained within a disc band of width dR at radius R is $dM = 2\pi R dR \times \Sigma_{\text{disc}}(R)$. However, we wish to compute the differential mass as a function of the equivalent volumetric density by spreading dM over the spherical shell of radius R and thickness dR . Hence, $dM = 4\pi R^2 dR \times \rho_{\text{disc}}(R)$. Thus, by equating the previous two expressions for the differential mass, the equation for the volumetric density of the disc is obtained:

$$\rho_{\text{disc}}(R) = \frac{1}{2R} \Sigma_{\text{disc}}(R) = \frac{1}{2R} \Sigma_0 e^{-R/R_d}. \quad (4)$$

Furthermore, to compute the total mass of the disc interior to a galactocentric radius, I integrate Equation 3 to yield:

$$M_{\text{disc}}(R) = 2\pi \Sigma_0 \int_0^R r e^{-r/R_d} dr = 2\pi \Sigma_0 R_d^2 \left[1 - e^{-R/R_d} \left(1 + \frac{R}{R_d} \right) \right]. \quad (5)$$

2.2 The central bulge

The Milky Way is classified as a barred spiral galaxy, meaning that rather than being perfectly radially symmetric, it has a boxy bulge of stars running through the middle. However, for the purposes of determining the large-scale mass distribution of the galaxy, this treatment will neglect the triaxial nature of the central region, replacing it with an equivalent radially symmetric distribution. Thus, I model the central bulge of the galaxy by normalizing the following formula, as shown by Binney et al. (1997) and utilized in McGaugh's adaptation (2008):

$$\rho_{\text{bulge}}(b) = \frac{\rho_{\text{bulge},0}}{\eta \zeta b_m^3} \frac{\exp \left[-(b/b_m)^2 \right]}{(1 + b/b_0)^{1.8}}, \quad (6)$$

with $b_m = 1.9$ kpc, $b_0 = 0.1$ kpc, $\eta = 0.5$, and $\zeta = 0.6$. In this equation, b is a radial parameter, with $b^2 = x^2 + \eta^{-2}y^2 + \zeta^{-2}z^2$, while b_m and b_0 are scaling parameters (analogous to the scale length discussed above for the disc). Because of the galaxy's triaxial boxy bulge, the density is not truly isotropic in R , the true radius, but may be expressed as isotropic in a new radial parameter, b , which is defined by scaling y and z by numerical factors η and ζ . In this way, η and ζ parameterize the extent of the anisotropic nature of the central bulge, i.e. how "boxy" it is. I normalize Equation 6 using the recommendation from McGaugh (2008): for consistency with the model of Bissantz, Englmaier & Gerhard (2003), I substitute R for b with no geometric scaling by $(\eta\zeta)^{1/3}$. This modification yields a softer bulge, with a density profile that drops off somewhat less steeply, with density equation:

$$\rho_{\text{bulge}}(R) = \frac{\rho_{\text{bulge},0}}{\eta \zeta b_m^3} \frac{\exp \left[-(R/b_m)^2 \right]}{(1 + R/b_0)^{1.8}}. \quad (7)$$

In Equations 6 and 7, I calculate the quantity $\rho_{\text{bulge},0} = 8.97 \times 10^{10} \text{ M}_\odot$ from $M_{\text{bulge}} = 1.10 \times 10^{10} \text{ M}_\odot$ for a choice of scale length of 2.5 kpc, based on the stipulations of the Tuorla-Heidelberg model (Flynn et al. 2006) as expressed by McGaugh (2008). One further note with regard to the bulge density function is that it is not analytically integrable, so to find $M_{\text{bulge}}(R)$, the total mass of the bulge interior to a radius, I use numerical integration of the form:

$$M_{\text{bulge}}(R) = 4\pi \int_0^R r^2 \rho_{\text{bulge}}(r) dr. \quad (8)$$

2.3 The galactic gas distribution

To find the gas distribution within the galaxy, I use the data found in table D1 of the study by Olling & Merrifield (2001), which provides disc surface densities of atomic and molecular hydrogen gas (H I and H₂, respectively) at specific galactocentric radii scaled by R_0 , the galactocentric radius of the Sun's orbit. By surface density, we are again using the convention of treating the galaxy as a flat disc. That is, the surface density at a given location denotes the differential mass of gas in a column of disc surface area dA , spanning the thickness of the galactic plane. (We will shortly convert this to a usual volumetric density, as was done for the stellar disc component.) For consistency with the velocity data in Section 3 of this paper, I use $R_0 = 8.5$ kpc, though the choice of R_0 should not greatly affect the final result of this work, since the gas comprises a relatively small fraction of the mass and the potential error in R_0 is comparatively small. In Olling & Merrifield's data, an additional $1.4 M_\odot \text{ pc}^{-2}$ of ionized gas is included at the solar radius, but at no other galactocentric radius. As suggested by McGaugh (2008), I subtract this $1.4 M_\odot \text{ pc}^{-2}$ from the value of the gas surface density at the solar radius, so that all data points uniformly measure only nonionized gas; this also allows for consistency with studies of other galaxies. Furthermore, as McGaugh suggests in his study, I multiply the sum of the atomic and molecular hydrogen components by 1.4 to accommodate the additional masses of heavier elements such as helium and the metals. I then plot the resulting data of surface density as a function of galactocentric radius and specify a best-fitting cubic polynomial passing through the origin (see Fig. 1). The surface density is defined to be zero at $R > 23.521$ kpc, to avoid nonphysical negative densities.

The gas distribution is thus given by the following formula (see Table 1 for constants G_i):

$$\Sigma_{\text{gas}}(R) = \begin{cases} \sum_{i=1}^3 G_i R^i & R \leq 23.521 \text{ kpc} \\ 0 & R > 23.521 \text{ kpc} \end{cases} \quad (9)$$

Similarly to the exponential disc distribution, this zone of gas can be normalized to a three-dimensional density function of radius, averaged over the entire sphere:

$$\rho_{\text{gas}}(R) = \frac{1}{2R} \Sigma_{\text{gas}}(R) = \begin{cases} \sum_{i=1}^3 \frac{G_i}{2} R^{i-1} & R \leq 23.521 \text{ kpc} \\ 0 & R > 23.521 \text{ kpc} \end{cases} \quad (10)$$

Also, as in the case of the exponential disc, I computed the function $M_{\text{gas}}(R)$, the total gas interior to a radius, via integration (see Table 1 for constants H_i):

$$M_{\text{gas}}(R) = 2\pi \int_0^R r \Sigma_{\text{gas}}(r) dr = \begin{cases} \sum_{i=3}^5 H_i R^i & R \leq 23.521 \text{ kpc} \\ H_6 & R > 23.521 \text{ kpc} \end{cases} \quad (11)$$

Table 1: Constants for model of galactic gas distribution.

i	G_i	H_i
1	2.7915×10^6	
2	-1.963×10^5	
3	3.3×10^3	5846503.92833
4		-308347.31895
5		4146.90230274
6		11556424162.9

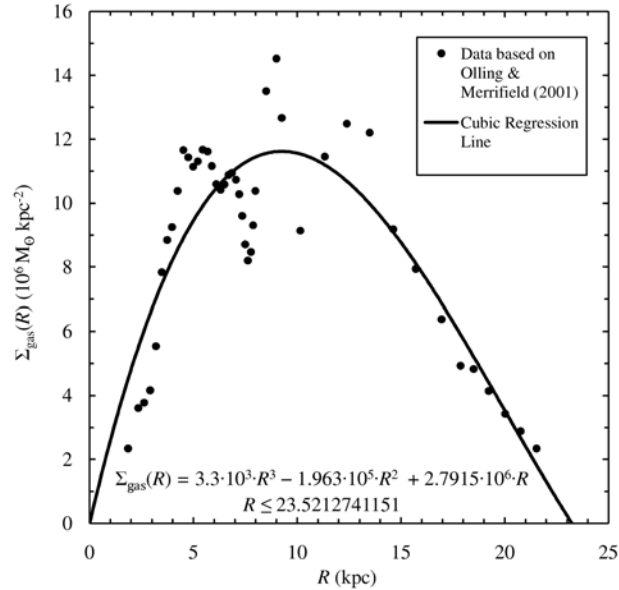


Figure 1: Total atomic and molecular gas surface density of the galaxy, based on the data from Olling & Merrifield (2001), along with the best-fitting cubic polynomial passing through the origin.

2.4 Total baryonic mass distribution

Thus, by summing the various components of baryonic matter, including luminous matter in stars as well as interstellar gas, the total distribution of the baryonic mass of the galaxy may be expressed. Specifically, the three-dimensional volumetric density of galactic baryonic matter may be formulated locally as a single explicit function:

$$\rho_{\text{model}}(R) = \rho_{\text{disc}}(R) + \rho_{\text{bulge}}(R) + \rho_{\text{gas}}(R). \quad (12)$$

Similarly, the total baryonic mass interior to a galactocentric radius may be expressed as:

$$M_{\text{model}}(R) = M_{\text{disc}}(R) + M_{\text{bulge}}(R) + M_{\text{gas}}(R). \quad (13)$$

See Fig. 2 for a visual summary of the galactic mass model and its components.

3 The Rotational Velocity Curve of the Galaxy

The rotational velocity curve of the Milky Way has been notoriously difficult to determine. Years of astronomical observation and multiple studies have been devoted to this task. While the velocity of the region interior to the solar radius is more accurately known, the curve at large distances is much less definite. For the present study, I use the function produced in the Massachusetts-Stony Brook galactic plane CO survey (Clemens 1985) for the velocity curve interior to 8.5 kpc. For the velocity curve at galactocentric radii greater than 8.5 kpc, I derive an exponential function based on the recent data from the study of the SDSS Blue Horizontal-Branch (BHB) stars by Xue et al. (2008). Together, these two studies, along with my calculations, provide a rotation curve of the galaxy at galactocentric radii of up to 55 kpc that is consistent with the best data at the present date. Note: all velocity functions $V(R)$ defined in this Section provide values in units of kilometers per second, where the

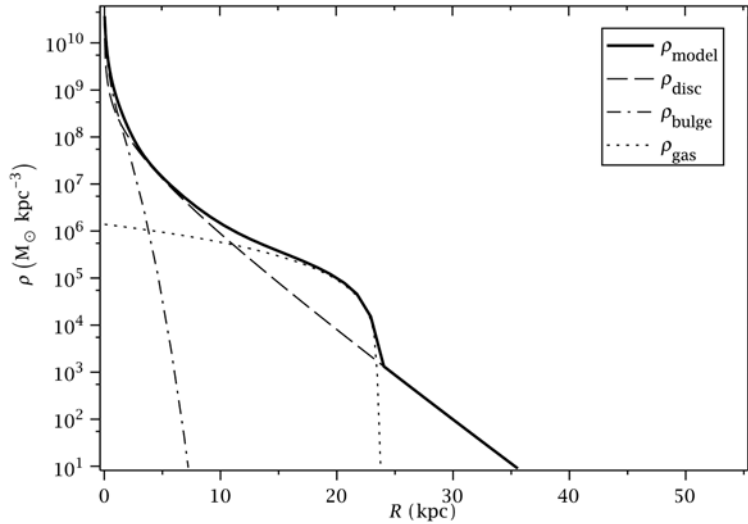


Figure 2: Summary of the mass model of the galaxy, with the three-dimensional volumetric density of each component and the total plotted as a function of galactocentric radius.

value of R is in kiloparsecs.

3.1 The rotation curve interior to 8.5 kpc

The Massachusetts-Stony Brook galactic plane CO survey provides quite precise data for radii interior to 8.5 kpc (see their fig. 3). Clemens incorporates data from not only the CO survey, but also H I, H II, and CO data from other sources. However, the error in the data from Clemens (1985) becomes alarmingly large at radii greater than 8.5 kpc. Thus, I use the best-fitting piecewise polynomial produced by Clemens (1985) for $R < 8.5$ kpc (see Fig. 3 for illustration and Table 2 for constants):

$$V(R) = \begin{cases} \sum_{i=0}^6 A_{1,i} R^i & R < 0.765 \text{ kpc} \\ \sum_{i=0}^5 A_{2,i} R^i & 0.765 \text{ kpc} \leq R < 3.825 \text{ kpc} \\ \sum_{i=0}^7 A_{3,i} R^i & 3.825 \text{ kpc} \leq R < 8.5 \text{ kpc} \end{cases} \quad (14)$$

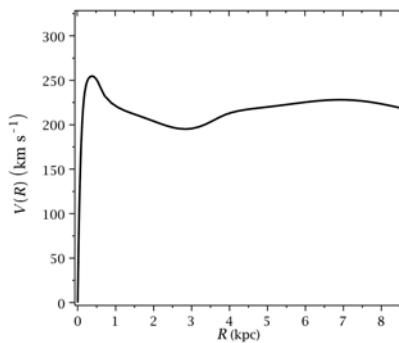


Figure 3: The rotational velocity curve interior to 8.5 kpc, as defined by Equation 14. This function is from the Massachusetts-Stony Brook galactic plane CO survey (Clemens 1985).

3.2 The rotation curve for large radii

Outside of 8.5 kpc, the radius of the Sun's orbit about the galactic center, the rotation curve is less certain. However, the recent study by Xue et al. (2008) allows for the definition of a fairly accurate curve as far as a galactocentric radius of 55 kpc. Using the data from their table 3, I defined the velocity at $R = 55$ kpc to be $\beta = V(55 \text{ kpc}) = 180 \text{ km s}^{-1}$, which is consistent with both models that Xue et al. (2008) use to interpret their data. Furthermore, I stipulate that the value and first derivative of the velocity curve at the Sun's orbit of 8.5 kpc match the values previously defined by the piecewise polynomial in Equation 14: $\alpha = V(8.5 \text{ kpc}) = 218.955757463 \text{ km s}^{-1}$ and $\gamma = V'(8.5 \text{ kpc}) = -9.597324992 \text{ km s}^{-1} \text{ kpc}^{-1}$. This is done to ensure continuity and differentiability of the new velocity curve, when combined with the results from the Massachusetts-Stony Brook galactic plane CO survey, as given in Equation 14. Thus, with the constants α , β , and γ , I define the following system of equations to solve for an exponential function for the velocity curve at $R > 8.5$ kpc, of the form $V(R) = A_4 e^{A_5 R} + A_6$:

$$\begin{cases} A_4 e^{8.5 A_5} + A_6 = \alpha \\ A_4 e^{55 A_5} + A_6 = \beta \\ A_4 A_5 e^{8.5 A_5} = \gamma \end{cases} \quad (15)$$

See Table 2 for the solution of this system. Equation 15 incorporates constraints drawn from the data of both Xue et al. and Clemens: the parameter β encompasses the result of Xue et al. (2008), while α and γ preserve smoothness and continuity of the velocity curve with that of Clemens (1985). A point of note is how well the exponential curve I have defined fits both models of the velocity data given by Xue et al. (2008) in their table 3. The model exponential curve I have defined corresponds to both of the data sets of Xue et al. for galactocentric radii greater than 8.5 kpc with a reduced χ^2 value of 0.85, indicating goodness of fit. Taking the error bars into account, the curve passes through the majority of the given entries in both models that Xue et al. use to represent their results. To summarize, as a result of my calculations in this Section, the velocity curve of the galaxy has been extended. It is represented as a piecewise function over a range of galactocentric radii of up to 55 kpc (see Fig. 4):

$$V(R) = \begin{cases} \sum_{i=0}^6 A_{1,i} R^i & R < 0.765 \text{ kpc} \\ \sum_{i=0}^5 A_{2,i} R^i & 0.765 \text{ kpc} \leq R < 3.825 \text{ kpc} \\ \sum_{i=0}^7 A_{3,i} R^i & 3.825 \text{ kpc} \leq R < 8.5 \text{ kpc} \\ A_4 e^{A_5 R} + A_6 & 8.5 \text{ kpc} \leq R < 55 \text{ kpc} \end{cases} \quad (16)$$

4 Results: Calculation of the Galactic Dark Matter Distribution

4.1 Calculation of the total galactic mass distribution

Using Equations 1 and 16, along with the definitions above, one may readily find that the total mass interior to a galactocentric radius is given by the following function (see Table 3 for the new constants and Fig. 5 for illustration):

$$M_V(R) = \begin{cases} \sum_{i=3}^{13} B_{1,i} R^i & R < 0.765 \text{ kpc} \\ \sum_{i=1}^{11} B_{2,i} R^i & 0.765 \text{ kpc} \leq R < 3.825 \text{ kpc} \\ \sum_{i=1}^{15} B_{3,i} R^i & 3.825 \text{ kpc} \leq R < 8.5 \text{ kpc} \\ R (B_4 + B_5 e^{A_5 R} + B_6 e^{2A_5 R}) & 8.5 \text{ kpc} \leq R < 55 \text{ kpc} \end{cases} \quad (17)$$

Furthermore, if $\rho_V(R)$ is defined as the total local three-dimensional volumetric density of all galac-

Table 2: Constants for the galactic rotational velocity function $V(R)$.

i	$A_{1,i}$	$A_{2,i}$	$A_{3,i}$
0	0	325.0912	-2342.6564
1	3069.81	-248.1467	2507.60391
2	-15809.8	231.87099	-1024.068760
3	43980.1	-110.73531	224.562732
4	-68287.3	25.073006	-28.4080026
5	54904	-2.110625	2.0697271
6	-17731		-0.08050808
7			0.00129348
<hr/>			
	A_4	A_5	A_6
	316.244380231	-0.246362129903	179.999587553

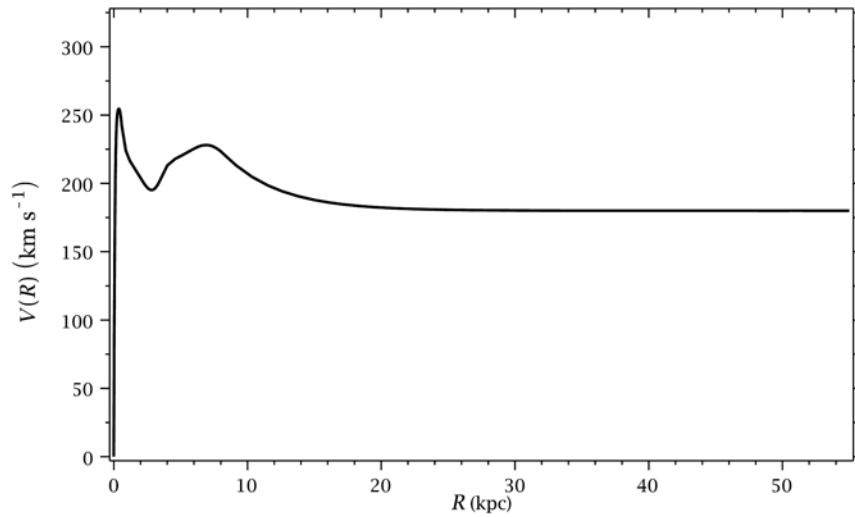


Figure 4: The full rotational velocity curve of the galaxy (Equation 16).

tic matter as a function of radius, as calculated from the velocity curve, then assuming a spherically symmetric mass distribution:

$$M_V(R) = 4\pi \int_0^R r^2 \rho_V(r) dr. \quad (18)$$

Equivalently,

$$\rho_V(R) = \frac{1}{4\pi R^2} \frac{d}{dR} (M_V(R))$$

$$= \begin{cases} \sum_{i=0}^{10} C_{1,i} R^i & R < 0.765 \text{ kpc} \\ \sum_{i=-2}^8 C_{2,i} R^i & 0.765 \text{ kpc} \leq R < 3.825 \text{ kpc} \\ \sum_{i=-2}^{12} C_{3,i} R^i & 3.825 \text{ kpc} \leq R < 8.5 \text{ kpc} \\ \frac{1}{4\pi} [B_4 R^{-2} + B_5 e^{A_5 R} (R^{-2} + A_5 R^{-1}) + B_6 e^{2A_5 R} (R^{-2} + 2A_5 R^{-1})] & 8.5 \text{ kpc} \leq R < 55 \text{ kpc} \end{cases} \quad (19)$$

Equation 19 is illustrated in Fig. 6. See Table 4 for new constants.

Thus, functions of the total mass distribution of the galaxy may be calculated and inferred from the rotational velocity curve (Equation 16).

Table 3: Constants for the function $M_V(R)$

i	$B_{1,i}$	$B_{2,i}$	$B_{3,i}$
1		24564047744.2	$1.27557704529 \times 10^{12}$
2		-37500168484.2	$-2.73078201846 \times 10^{12}$
3	$2.19034486335 \times 10^{12}$	49352771367.2	$2.57674025074 \times 10^{12}$
4	$-2.25609495184 \times 10^{13}$	-43481386377.7	$-1.43828292011 \times 10^{12}$
5	$1.20856086239 \times 10^{14}$	29059006683.2	536455819305
6	$-4.20670428948 \times 10^{14}$	-15147014255.6	-142270621544
7	$1.02978778528 \times 10^{15}$	5796118507.53	27744819989.6
8	$-1.82490561972 \times 10^{15}$	-1518158230.29	-4046039381.34
9	$2.33664373715 \times 10^{15}$	254764268.883	443464513.413
10	$-2.10536449516 \times 10^{15}$	-24600106.3077	-36352078.8409
11	$1.26349411608 \times 10^{15}$	1035408.34664	2193858.98095
12	$-4.5253973374 \times 10^{14}$		-94540.2910909
13	$7.30728363957 \times 10^{13}$		2750.99016397
14			-48.4081726383
15			0.388874030682
<hr/>			
	B_4	B_5	B_6
	7530651076.8057	26461461549.993	23245299118.903

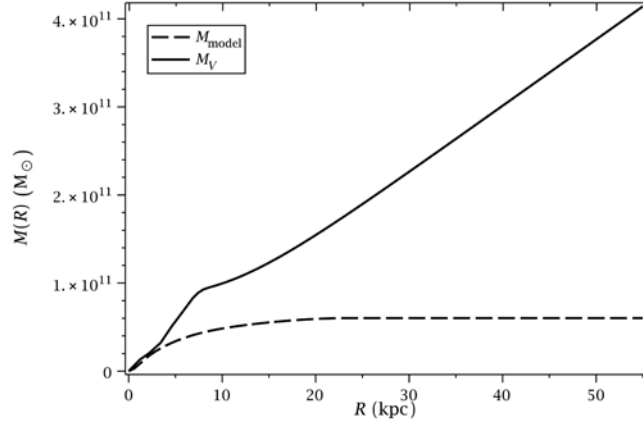


Figure 5: An illustration of the discrepancy between the mass interior to a galactocentric radius as predicted by the velocity curve (M_V), as opposed to the mass accounted for in the galactic mass model (M_{model}).

4.2 Calculation of the dark matter distribution

In this Section, I define $\rho_{\text{DM}}(R)$, the three-dimensional volumetric density distribution of dark matter, as $\rho_V(R) - \rho_{\text{model}}(R)$, and similarly, $M_{\text{DM}}(R) = M_V(R) - M_{\text{model}}(R)$. Thus, I have calculated the dark matter density distribution of the Milky Way Galaxy, expressed as a single function:

$$\rho_{\text{DM}}(R) = \begin{cases} \sum_{i=0}^{10} C_{1,i} R^i & R < 0.765 \text{ kpc} \\ \sum_{i=-2}^8 C_{2,i} R^i & 0.765 \text{ kpc} \leq R < 3.825 \text{ kpc} \\ \sum_{i=-2}^{12} C_{3,i} R^i & 3.825 \text{ kpc} \leq R < 8.5 \text{ kpc} \\ \frac{1}{4\pi} [B_4 R^{-2} + B_5 e^{A_5 R} (R^{-2} + A_5 R^{-1}) + B_6 e^{2A_5 R} (R^{-2} + 2A_5 R^{-1})] & 8.5 \text{ kpc} \leq R < 55 \text{ kpc} \end{cases}$$

$$- \left\{ \frac{1}{2R} \Sigma_0 e^{-R/R_d} + \frac{\rho_{\text{bulge},0}}{\eta \zeta b_m^3} \frac{\exp[-(R/b_m)^2]}{(1+R/b_0)^{1.8}} + \begin{cases} \sum_{i=1}^3 \frac{G_i}{2} R^{i-1} & R \leq 23.521 \text{ kpc} \\ 0 & R > 23.521 \text{ kpc} \end{cases} \right\}. \quad (20)$$

Furthermore, the total mass of dark matter interior to a given galactocentric radius may be expressed by the function:

$$M_{\text{DM}}(R) = \begin{cases} \sum_{i=3}^{13} B_{1,i} R^i & R < 0.765 \text{ kpc} \\ \sum_{i=1}^{11} B_{2,i} R^i & 0.765 \text{ kpc} \leq R < 3.825 \text{ kpc} \\ \sum_{i=1}^{15} B_{3,i} R^i & 3.825 \text{ kpc} \leq R < 8.5 \text{ kpc} \\ R (B_4 + B_5 e^{A_5 R} + B_6 e^{2A_5 R}) & 8.5 \text{ kpc} \leq R < 55 \text{ kpc} \end{cases} - 2\pi \Sigma_0 R_d^2 \left[1 - e^{-R/R_d} \left(1 + \frac{R}{R_d} \right) \right]$$

$$- 4\pi \frac{\rho_{\text{bulge},0}}{\eta \zeta b_m^3} \int_0^R r^2 \frac{\exp[-(r/b_m)^2]}{(1+r/b_0)^{1.8}} dr - \begin{cases} \sum_{i=3}^5 H_i R^i & R \leq 23.521 \text{ kpc} \\ H_6 & R > 23.521 \text{ kpc} \end{cases}. \quad (21)$$

These calculations are depicted graphically in Figs. 7, 8, and 9. Note in Fig. 7 that the density of galactic dark matter decreases faster than a density profile $\propto R^{-2}$, since the velocity curve decreases somewhat at large galactocentric radii before leveling off; a density profile proportional to R^{-2} would

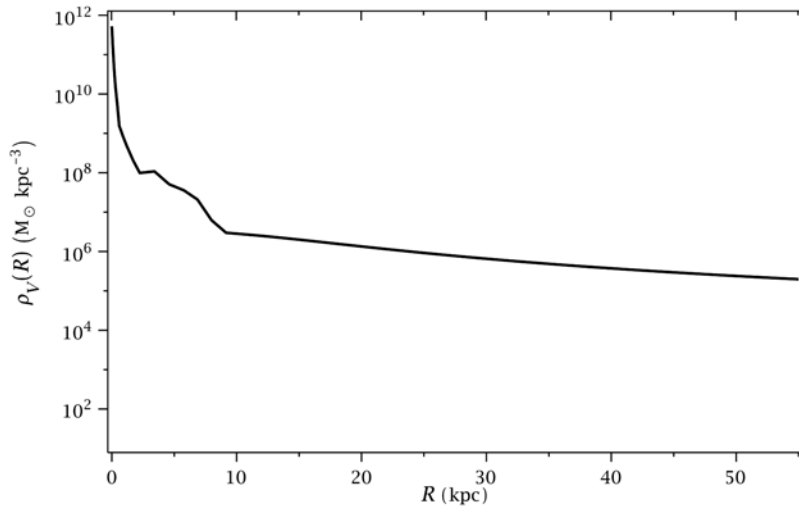


Figure 6: The three-dimensional volumetric density of the total matter in the galaxy as a function of galactocentric radius, based on the rotational velocity curve.

be consistent with a constant rotational velocity. Similarly, in Fig. 8, one may observe that the mass of dark matter interior to a galactocentric radius increases almost linearly with distance. Both of these observations are consistent with the concept of a galaxy dominated by dark matter, especially at large radii, a hypothesis supported by Fig. 9.

A further item of note is the irregular behavior of the predicted density of dark matter at galactocentric radii smaller than approximately 2.5 to 3 kpc. Within this region, the dark matter density curve behaves anomalously, predicting negative values, then reaching high positive densities near the very center of the galaxy. These odd effects are explained, however, by the complex nature of the galactic center. The mass model I use is radially symmetric, while in fact the galaxy has a triaxial, boxy bulge at the center, leading to noncircular orbital motions and the destruction of the radial symmetry of the velocity curve. Thus, the supposed negative density of dark matter interior to 3 kpc is simply due to the fact that matter at this radius is rotating more slowly than what would be expected from the mass model. Likewise, the unexpectedly high predicted dark matter density values near the galactic center simply denote the fact that matter at the very center of the galaxy rotates faster than what would be expected from the observable matter, possibly a consequence of the supermassive central black hole. For clarity, the anomalous values in the center of the galaxy have been truncated from the graphs in Figs. 7 through 9.

Overall, the velocity data demand that a total mass of approximately $4.14 \times 10^{11} M_{\odot}$ is contained within a galactocentric radius of 55 kpc. However, the mass model only accounts for a mass of approximately $6.03 \times 10^{10} M_{\odot}$ inside this radius. Thus, of the total mass of the galaxy interior to a 55 kpc radius, approximately 14.5 percent is contained in observable baryonic matter, while the remaining 85.5 percent is dark matter (see Fig. 9). The dark matter halo of the Milky Way thus has a mass interior to 55 kpc of approximately $3.54 \times 10^{11} M_{\odot}$. The extent to which this halo extends beyond 55 kpc is unclear, but it is evident from these calculations that dark matter dominates the composition of the galaxy. This study thus provides significant new insight into the distribution of galactic dark matter, while quantitatively confirming at the local galactic level the generally accepted belief that dark matter is the main component of matter in the universe as a whole.

A further intriguing calculation involves the comparison of the density of galactic dark matter to the overall average dark matter density of the universe. Using the value provided by Fukugita & Peebles (2004), the energy density of dark matter in the universe is: $\Omega_{DM} = 0.23$, or alternatively,

Table 4: Constants for the function $\rho_V(R)$

i	$C_{1,i}$	$C_{2,i}$	$C_{3,i}$
-2		1954744810.42	101507196026
-1		-5968337181.04	-434617456744
0	522906318117	11782106277.6	615151421954
1	$-7.1813732734 \times 10^{12}$	-13840555149	-457819672600
2	$4.80871088192 \times 10^{13}$	11562211387.4	213448988482
3	$-2.00855334539 \times 10^{14}$	-7232166575.59	-67929218026.5
4	$5.7363535727 \times 10^{14}$	3228683189.27	15455038362.9
5	$-1.16177100022 \times 10^{15}$	-966489546.985	-2575788669.94
6	$1.67349780455 \times 10^{15}$	182461467.222	317608062.28
7	$-1.67539583207 \times 10^{15}$	-19576142.5973	-28928065.196
8	$1.10600233778 \times 10^{15}$	906346.960675	1920399.25696
9	$-4.32143613421 \times 10^{14}$		-90279.3278908
10	$7.55943702678 \times 10^{13}$		2845.91893945
11			-53.93079973
12			0.464184181673

$\rho_{\text{DM}} = 0.23\rho_{\text{c0}}$, where the density parameter $\Omega = 1$, meaning that the density of the universe in the present epoch equals the present critical density, given by Binney & Tremaine (2008) as $\rho_{\text{c0}} = 1.3599 \times 10^5 \text{M}_{\odot} \text{kpc}^{-3}$, assuming consistently with Fukugita & Peebles (2004) that the Hubble constant is exactly $70 \text{ km s}^{-1} \text{ Mpc}^{-1}$. Thus, $\rho_{\text{DM}} = 3.1278 \times 10^4 \text{M}_{\odot} \text{kpc}^{-3}$, a value that is significantly lower than the density of dark matter within a galactocentric radius of 55 kpc, though comparable to the galactic dark matter density at large radii (see Table 5 for specific values). Therefore, as compared to the universe as a whole, the galaxy is a relatively compact object, but not excessively dense.

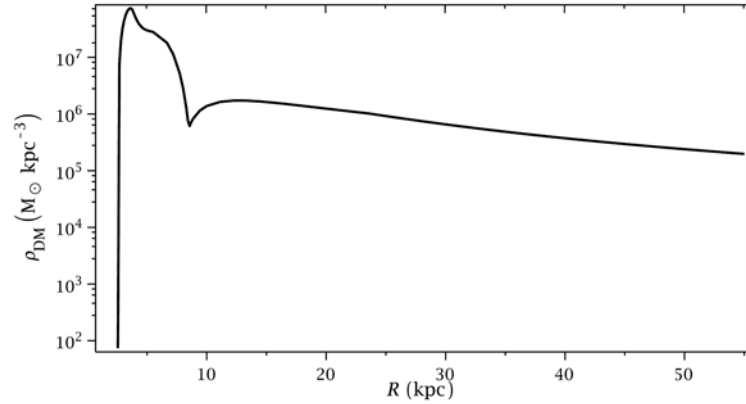


Figure 7: The density of dark matter in the Milky Way Galaxy as a function of galactocentric radius (Equation 20). Note the gradual decline of the density curve at large radii (see Table 5).

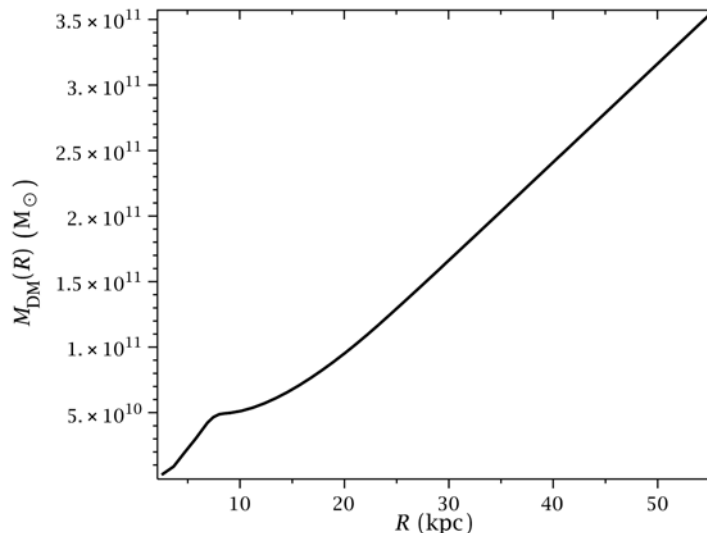


Figure 8: The total mass of dark matter interior to a galactocentric radius. Note the linearity of the function at great distances from the galactic center, implying the domination of dark matter.

5 The Role of Neutrinos

Neutrinos have often been proposed as a component of dark matter and therefore are of interest in an examination of the effects of dark matter within the galaxy. Long thought to be massless, relatively recent experiments have proven that neutrinos do, in fact, possess a small mass. Thus, neutrinos create a gravitational effect. In this Section, I estimate the validity of the proposition of neutrinos as candidate dark matter particles within the Milky Way Galaxy.

There exist three types, or flavors, of neutrinos, and experiments have not yet been able to determine the specific mass of any particular flavor. However, the sum of the masses of the three flavors has been estimated using cosmological constraints not to exceed 0.3 eV (Goobar et al. 2006).

To calculate the gravitational effect of neutrinos, one must initially determine the density of neutrinos within the galaxy. To astrophysical accuracy, one can show that the density of neutrinos throughout space can be approximated as a constant. This can be understood by considering the energy of a single neutrino of average energy from the Cosmic Neutrino Background (CνB), the inundation of neutrinos left over from the Big Bang that fills all of space, similar to the Cosmic Microwave Background (CMB). By treating neutrinos as relativistic radiation particles, which is a common method used in this type of calculation, one can show that the effective temperature of the CνB is given by:

$$T_\nu = \left(\frac{4}{11}\right)^{1/3} T_\gamma, \quad (22)$$

where T_γ is the temperature of the CMB (Mangano et al. 2008). Using a value of $T_\gamma = 2.725$ K (Fixsen & Mather 2002), Equation 22 yields a value of $T_\nu = 1.945$ K. Thus, one can assert that the energy of the neutrino is:

$$E_\nu = \frac{3}{2}kT_\nu = 2.514 \times 10^{-4} \text{ eV}, \quad (23)$$

using the latest (2006) value of Boltzmann's constant, $k = 1.3806504 \times 10^{-23}$ J K⁻¹, and the electron volt, $1.602176487 \times 10^{-19}$ J, given by CODATA and NIST (Mohr et al. 2007).

However, one can also compute the gravitational potential energy difference that the neutrino

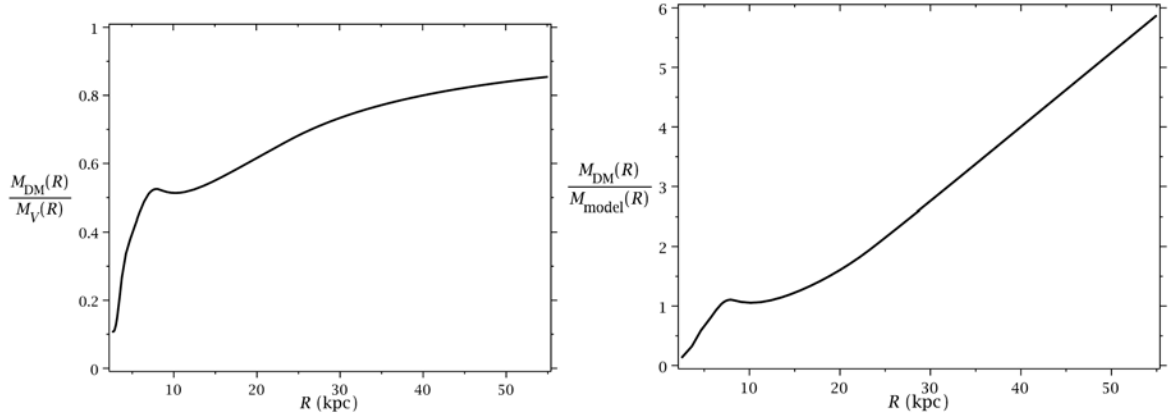


Figure 9: (left) The ratio of dark matter to total matter in the galaxy. Note that the curve levels off somewhat as the dark matter density decreases, reaching a value of about 85 percent dark matter interior to 55 kpc. (right) The ratio of dark matter to baryonic matter, illustrating the dominance of dark to baryonic components in the composition of the Milky Way.

gains as it falls from deep space (essentially, an infinite distance) towards the center of the galaxy, taking into account only the galactic mass within the radius of 55 kpc. Since the masses of the three flavors of neutrinos are not known, this average neutrino will be taken to possess a mass of one third the total mass, or $m_\nu = 0.1$ eV (which is equivalent to 1.783×10^{-37} kg). Thus, the gravitational potential energy difference is given by:

$$\Delta U = 4\pi G m_\nu \int_0^{55} \frac{\rho_V(r)r^2}{r} dr = 6.204 \times 10^{-26} \text{ J} = 3.872 \times 10^{-7} \text{ eV}. \quad (24)$$

As one can see, $\Delta U \ll E_\nu$, so any kinetic energy that the neutrino gains in falling toward the Milky Way is negligible compared to the energy that the neutrino possesses as a result of its temperature, by Equation 23. Thus, the neutrino is not bound to the galaxy and its orbit has a large positive total energy, indicating that the gravitational effect of the galaxy has only a small effect on the distribution of cosmic neutrinos. Therefore, for the purposes of this study, the neutrino density can be asserted to be constant.

As shown by Lopez et al. (1999) and Mangano et al. (2008), the energy density of cosmic neutrinos and photons are related by the equation:

$$\rho_\nu = \frac{7}{8} \left(\frac{4}{11} \right)^{4/3} N_\nu \rho_\gamma, \quad (25)$$

where N_ν is the effective number of neutrinos. When oscillations between the three flavors of massive neutrinos are taken into account, $N_\nu = 3.046$ (Mangano et al. 2008).

Since the CMB radiation can be treated as that of a blackbody, the energy density of the CMB may be found thus:

$$\rho_\gamma = \frac{4\sigma T_\gamma^4}{c} = 4.172 \times 10^{-14} \text{ J m}^{-3}. \quad (26)$$

Thus, $\rho_\nu = 2.886 \times 10^{-14} \text{ J m}^{-3}$. Here, the value of the Stefan-Boltzmann constant σ is the CODATA (2006) value of $5.670400 \times 10^{-8} \text{ W m}^{-2} \text{ K}^{-4}$ (Mohr et al. 2007). The speed of light is the defined value of $299792458 \text{ m s}^{-1}$.

Using this neutrino energy density, along with the energy of our single average neutrino (Equation

Table 5: Selected values of the predicted density of galactic dark matter at various radii (Equation 20).

R (kpc)	ρ_{DM} ($M_{\odot} \text{ kpc}^{-3}$)
3	3.7139×10^7
5	2.9909×10^7
8	2.9630×10^6
8.5	5.6253×10^5
10	1.3843×10^6
12	1.7183×10^6
15	1.6304×10^6
20	1.2454×10^6
25	9.2106×10^5
30	6.5652×10^5
35	4.8683×10^5
40	3.7393×10^5
45	2.9578×10^5
50	2.3967×10^5
55	1.9809×10^5

23), one may find the number density of neutrinos:

$$n_{\nu} = \frac{\rho_{\nu}}{E_{\nu}} = 7.164 \times 10^8 \text{ m}^{-3}, \quad (27)$$

which can readily be converted into a mass density:

$$\mu_{\nu} = m_{\nu} n_{\nu} = 1.277 \times 10^{-28} \text{ kg m}^{-3} = 1.886 M_{\odot} \text{ kpc}^{-3}. \quad (28)$$

The neutrino densities calculated in this Section are consistent with the results of Fukugita & Peebles (2004), taking into account the uncertainty inherent in the neutrino mass estimate.

As one can see by comparison with the values of the predicted dark matter density in Fig. 7, neutrinos can only comprise a very small fraction of galactic dark matter and do not nearly account for the observed quantities of dark matter present in the galaxy.

6 Conclusions

The observed mass and the observed rotational velocity curve of the Milky Way Galaxy are seemingly inconsistent without the addition of dark matter. As I have shown, the galaxy's rotational velocity levels off at large distances, rather than falling in the characteristic Keplerian fashion, implying the existence of large quantities of invisible dark matter.

Through the development of a mass model of the galaxy and an analysis of the rotational velocity curve, I have been able to produce an estimate of the dark matter content of the Milky Way. Interior to a galactocentric radius of 55 kpc, the $\sim 4 \times 10^{11} M_{\odot}$ of matter in our galaxy is roughly 85 percent dark (or approximately $3.5 \times 10^{11} M_{\odot}$ is dark matter). The results of this study provide a new and detailed glimpse into the dark matter structure of the galaxy, while maintaining consistency with conventional astrophysical theory on the subject, which holds that dark matter makes up the majority of all matter in the universe.

The galactic mass model employed followed mainly from the Tuorla–Heidelberg model (Flynn et al. 2006), with an exponential stellar disc and central stellar bulge. In addition, the model incorporated my calculation of the distribution of gas in the galaxy, from data supplied by Olling & Merrifield

(2001). The data for the velocity curve consisted of two main parts: the inner curve is represented as a piecewise function from the Massachusetts-Stony brook CO survey (Clemens 1985), while the outer rotation curve is a function I derived based on data from the study by Xue et al. (2008).

More importantly, I have been able to quantitatively determine the distribution of dark matter within our galaxy. This distribution follows a pattern roughly inversely proportional to the square of the galactocentric radius, but the curve contains some interesting complexities that may serve as grounds for future study in this area. The results of this study are relevant for any experiment or theoretical discussion involving the dark matter content of the galaxy. In experimental investigation, a knowledge of the local dark matter density is conducive to decisive detection of particles proposed as dark matter candidates. In the theoretical realm, the dark matter distribution could lend insight into the dynamics of galaxy formation and evolution.

Finally, through a discussion of the properties of neutrinos and various calculations, I demonstrated that, given the data from the Cosmic Neutrino Background, as well as current constraints on neutrino mass, neutrinos can only account for a small component of the dark matter necessary to create the rotation of the galaxy. The search for the true nature of dark matter continues, broadening our understanding of the fundamental nature of the universe.

Acknowledgments

I would like to thank my research mentor, Dr. Thomas Walsh, of the University of Minnesota, for all of his constructive advice. I am further thankful for helpful communication with Dr. Stacy S. McGaugh of the University of Maryland.

References

- [1] Binney J., Tremaine S., 1987, Galactic Dynamics. Princeton Univ. Press, Princeton, NJ
- [2] Binney J., Tremaine S., 2008, Galactic Dynamics, Second Ed. Princeton Univ. Press, Princeton, NJ
- [3] Binney J., Gerhard O., Spergel D., 1997, MNRAS, **288**, 365
- [4] Bissantz N., Englmaier P., Gerhard O., 2003, MNRAS, **340**, 949-968
- [5] Clemens D. P., 1985, ApJ, **295**, 422-436
- [6] Fixsen D. J., Mather, J. C., 2002, ApJ, **581**, 817-822
- [7] Flynn C., Holmberg J., Portinari L., Fuchs B., Jahreiß H., 2006, MNRAS, **372**, 1149-1160
- [8] Fukugita M., Peebles, P. J. E., 2004, ApJ, **616**, 643-668
- [9] Goobar A., Hannestad S., Mörtsell E., Tu H., 2006, J. Cosmol. Astropart. Phys., JCAP **06** (2006) 019
- [10] Lopez R. E., Dodelson S., Heckler A., Turner M. S., 1999, Phys. Rev. Lett., **82**, 3952-3955
- [11] McGaugh S. S., 2008, ApJ, **683**, 137-148
- [12] Mangano G., Miele G., Pastor S., Pinto T., Pisanti O., Serpico P. D., 2005, Nucl. Phys. B, **729**, 221-234
- [13] Mohr P. J., Taylor B. N., Newell D. B., 2007, CODATA Recommended Values of the Fundamental Physical Constants: 2006. NIST, Gaithersburg, MD
- [14] Olling R. P., Merrifield M. R., 2001, MNRAS, **326**, 164-180
- [15] Seidelmann P. K., United States Naval Observatory 2005, Explanatory Supplement to the Astronomical Almanac. University Science Books, Nautical Almanac Office, Great Britain
- [16] Williams D. R., 2004, Sun Fact Sheet. NASA Goddard Space Flight Center, Greenbelt, MD
- [17] Xue X.-X., Rix H.-W., Zhao G. et al. 2008, ApJ, **684**, 1143-1158

Simulation of Metallic Structure in an Electric Field

Calvin Wylie*

Advisor: Dr. James H. Taylor†

Department of Biochemistry, Chemistry, and Physics
University of Central Missouri
Warrensburg, MO 64093

August 7, 2009

Key Words: valence electrons, metals, computer simulation, Monte Carlo, Coulomb interaction, electric field, kinetic theory

Abstract

We explore a question about how the structure and strength of a metal is affected by an electric field. Specifically: “Is the metal weakened in the presence of an electric field?” Using a computer simulation we calculate the positions of metal ions based on some initial conditions. The simulation is set up to calculate this in two ways: a Coulomb force calculation and a Monte Carlo method. In electromagnetic theory, we treat the valence electrons in a metal as free particles within a conducting-material ion lattice. The metal is held together by interactions between these ions and electrons. When an electric field is put into place, the electrons can move relatively freely due to the force from the electric field. If a strong enough electric field were applied, we would have an under-abundance of electrons in one area of the metal and an over-abundance elsewhere. Since the structure of the metal relies on the electron-ion interactions, if we change the ratio of ions to electrons in a given area, we expect it to affect the strength of the metal’s structure near the surface as well as a small increase in separation between the ions along the direction of the field. We tested this hypothesis via computer simulation.¹

1 Introduction

With the growing interest in nanotechnology, there is a need to understand the specific aspects of materials on the molecular level. The purpose of this research is to examine the surface properties of single-element metals. As with most modern conceptions of metallic structure, we regard a metal as a “gas” or “sea” of approximately free valence electrons scattered throughout a lattice of positively charged ions [1]. It is the electromagnetic interaction of these positive and negative charges that bind the atoms of the metal together. Since we

*CalWylie@gmail.com

†jtaylor@ucmo.edu

¹This project was presented by Wylie at the 2009 Honors Symposium at the University of Central Missouri.

regard the valence electrons as a collection of relatively free charges, they can be influenced by an electric field and travel within the confines of the metal lattice. If we were to apply an external static electric field, the electrons should rapidly reorient themselves such that the magnitude of the electric field in the interior of the metal is zero, as predicted from electrostatic theory [2]. It is this static condition we wish to look at in further detail. Because the static electric field must be zero inside the metal, we expect a build-up of electrons on the surface of the metal near where the electric field lines enter the metal, and a deficiency of electrons on the surface of the metal where the field lines exit, as seen in Figure 1:

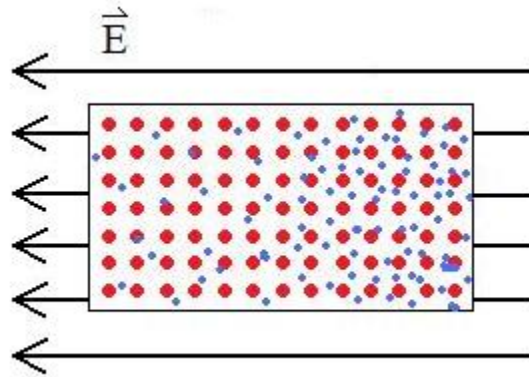


Figure 1: The red dots represent ions, and the blue represent electrons. The electron density on the right-hand side where the electric field lines enter is much greater than that of the left.

The electron-deficient metallic surface is the focus of this research. Because of the lower density of negative charge, there are fewer attractive interactions between oppositely charged ions and electrons, thereby allowing a stronger repulsive interaction between ions. With this increased repulsion, we expect to observe a separation of ions in the surface of the metal near this electron deficiency. We calculate the average separation between neighboring ions at the vertices of each metallic unit cell, along directions parallel and perpendicular to the surface of the metal. The results are reported as the average percent change of all such distance separations.

For our situation, we have created a computer program that calculates the position and movement of the electrons and ions for various elemental metals. The program uses two common simulation methods to perform these calculations: a particle dynamics (PD) simulation and a Monte Carlo (MC) simulation. The program allows the user to change the type of metal by changing the properties used in the calculations of particle movement. These properties are: the ionic charge, the ionic radius, the lattice constant², the ionic mass, the crystal structure of the metal, the work function of the metal, and the temperature. All the tests conducted in this research used ⁶³Cu (copper) as the metal, with a temperature of 273 K.

²The lattice constants are the edge lengths of a single unit cell in a crystal structure. Because all the metals in this project have cubic structure, the edge lengths are all the same; thus, only one lattice constant is needed. In other words, the lattice constant is the distance between nearest neighbor ions.

The user can also change the initial dimensions of the lattice and the electron density³. The program collects data after a certain user-defined number of simulation iterations, recording the average change in ion separation parallel and perpendicular to the surface. For testing, the program can automatically change the electron density at a user-defined time as well, simulating the activation of an external electric field.

Both simulation types are initialized in the same manner: the program generates a lattice of ions using the given properties of the metal, then fills the lattice volume with a number of randomly positioned electrons such that the situation is electrically neutral (We decrease the electron density to simulate the application of an electric field later). The particles start with velocities in random directions, with magnitudes equal to the average speed of a particle given by the kinetic theory of matter [1]:

$$v = \sqrt{\frac{3k_bT}{m}}, \quad (1)$$

where k_b is the Boltzmann constant, T is the absolute temperature, and m is the mass of the particle. From these initial conditions, the program then executes either a PD or MC simulation to calculate the movement and position of each particle. In both simulations, all particles (both the ions and electrons) are free to move under the influence of all the other particles and their movement restricted only by their own mass.

Because the scale of the simulation is limited by the processing power of the computer, we employ slab boundary conditions (SBC), a special case of periodic boundary conditions (PBC), to simulate the seemingly infinite expanse of unit cells in the crystal structure of a metal [3]. We will call the volume in which the simulation proper takes place the “simulation box.” We assume the electrostatic conditions are similar across the surrounding metallic surface, so we effectively tile copies of the simulation box; the repeated boxes are “images” of the simulation box. Figure 2 gives a visualization of this concept. For SBC, we apply PBC to all sides of the simulation box except the sides parallel to the surface of the metal (the “top” and “bottom” boundaries, see Figure 2). The box is centered on the generated lattice and extends to one-half of the lattice constant beyond the extreme outward-most ions, except for the top boundary, which extends to an arbitrarily chosen height of three times the depth simulated from the metal surface; this ensures there is a sufficient vacuum above the surface of the metal, to simulate the “emptiness” outside the surface of the metal. There are two PBC that are applied to the “sides” of the simulation box: boundary continuity and the minimum image criterion. We accomplish boundary continuity by looping the simulation space: if a particle moves outside the simulation box of length L , we reposition it near the opposing face of the simulation box by adding or subtracting L from the position. The minimum image criterion states that for a particle A in a simulation box, for any interactions with another particle B we use the closest image of the B, and ignore all other images; this models the interaction with particles outside the simulation box. For example, if the distance between two particles is greater than $\frac{L}{2}$, we add or subtract L to the distance such that the interaction

³If ρ_0 is the density of free electrons such that the bulk metal is electrically neutral, the percentage P describes the modified electron density ρ used in the simulation such that: $\rho = P\rho_0$, $0 \leq P \leq 1$. The user changes the value of P and the program calculates ρ . Based on the desired P , the appropriate number of electrons to give an electron density of ρ are used in updating the program.

is between one particle inside the simulation box and a closer image of the other particle outside. Figure 2 gives a visualization of PBC:

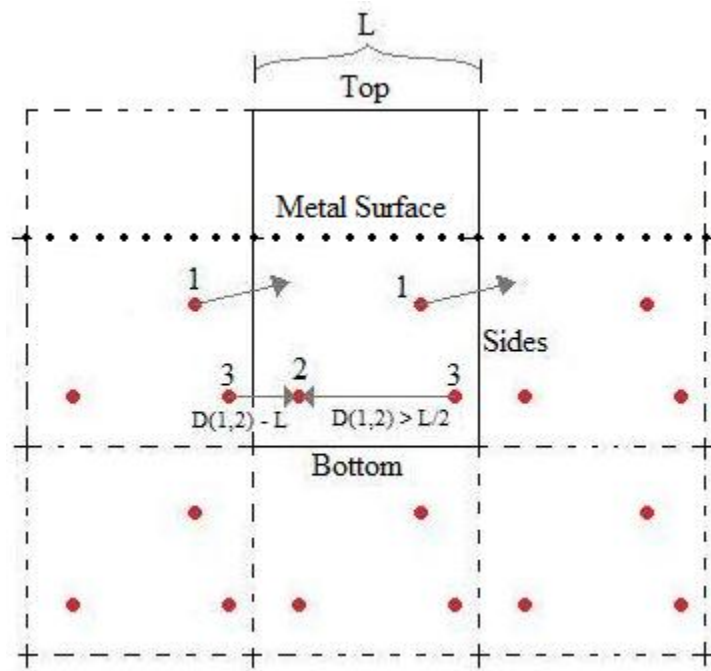


Figure 2: Diagram of SBC. The simulation box is identified by the solid lines, the images by dashed lines, and the metal surface by the dotted line. Both PBC are indicated. The particle 1 displays boundary continuity: as the particle in the simulation box leaves, its neighboring image takes its place. Particles 2 and 3 demonstrate the minimum image criterion: the distance between particles 2 and 3 in the simulation box is greater than $\frac{L}{2}$, so particle 2 interacts with the closest image of particle 3 (to its left) instead of the “real” particle 3 (to its right, in the simulation box).

Unlike side boundaries, the top and bottom boundaries are not treated with the same PBC. At the bottom boundary, we employ the minimum image criterion to simulate the expanse of particles in the interior of the metal, but do not use the continuity condition. Instead, if a particle crosses the bottom boundary, the component of its velocity perpendicular to the surface is reversed, and it is given a random position on the bottom boundary. This simulates a particle leaving the simulation box, and another entering in a different position. The metal surface has no boundary conditions and is open, except for the work function applied here. In case a particle has enough kinetic energy to overcome the work function, at the top of the simulation box, the component of velocity perpendicular to the metal’s surface is reversed. The reversal of velocity on the top and bottom boundaries ensures the total number of particles in the simulation remains constant.

To simulate the activation of an external electric field, the number of electrons in the simulation can be changed to a percentage P of the number of electrons required to be electrically neutral. Those electrons that are removed are stored at a location outside the simulation box and are disabled, meaning they are no longer used in any calculations of

the simulation. In this simulation, there are no direct calculations of the effects of the electric field itself, we only simulate it through the decreased electron density. The reason for this method of simulation is the additional complications with the boundary conditions to maintain a constant number of particles.

As a note, because of the small scale of the simulation, the units used in calculation are as follows:

In Simulation	SI Value
unit length	1 angstrom (Å) = 10^{-10} m
unit mass	electron mass (m) = 9.11×10^{-31} kg
unit charge	electron charge ($-e$) = -1.602×10^{-19} C
unit time	1 attosecond (as) = 10^{-18} s

Accordingly, the physical constants such as Coulomb's constant k_e and the Boltzmann constant k_b have been changed to match this scale: $k_e = \frac{1}{4\pi\epsilon_0} = 2.532 \times 10^{-4} \frac{m^3}{e^2(as)^2}$, and $k_b = 1.515 \times 10^{-9} \frac{m}{K(as)^2}$.

2 Particle Dynamics

The first type of simulation is the particle dynamics simulation [4]. We expect this simulation to be deterministically accurate as the system of particles evolves through time. It is based on classical laws of physics: Coulomb's law ($\vec{F}_c = k_e \frac{q_1 q_2}{r_{1 \rightarrow 2}^2} \hat{r}_{1 \rightarrow 2}$ where q_1 and q_2 are the charges, $\hat{r}_{1 \rightarrow 2}$ is a unit vector in the direction from charge 1 to charge 2, $r_{1 \rightarrow 2}$ is the distance between two interacting particles, and $k_e = \frac{1}{4\pi\epsilon_0}$, where ϵ_0 is the permittivity of free space), Newton's second law ($\vec{F}_{net} = \sum \vec{F}_c = m\vec{a}$, where m is the mass of a particle, \vec{a} is its acceleration, and \vec{F}_{net} is the net force), and the equations of motion ($\Delta\vec{v} = \int_{t_1}^{t_2} \vec{a} dt$ and $\Delta\vec{s} = \int_{t_1}^{t_2} \vec{v} dt$, where \vec{v} and \vec{s} are the velocity and position vectors, respectively). By adding all the Coulomb interactions together, we can find the net force on a particular particle j at an instant in time due to the interactions with all the other particles:

$$\vec{F}_j = \sum_{i=1}^N \vec{F}_{i \rightarrow j} = k_e \sum_{i=1}^N \frac{q_1 q_2}{r_{i \rightarrow j}^2} \hat{r}_{i \rightarrow j}, \quad (2)$$

where N is the total number of particles in the simulation and $i \neq j$. Using Eq. (2) and Newton's second law, $a_j = \frac{\sum_{i=1}^N \vec{F}_{i \rightarrow j}}{m_j}$, we can calculate the acceleration of each particle at every step in the simulation. Using the common approximation of the antiderivatives in the equations of motion:

$$\vec{v} = \vec{a}\Delta t + \vec{v}_0 \quad (3)$$

and

$$\vec{s} = \vec{v}\Delta t + \vec{s}_0, \quad (4)$$

we can calculate the new velocities and positions of each particle in the simulation, where \vec{v}_0 and \vec{s}_0 are the initial velocity and position at the beginning of a reasonably small time interval Δt . For all simulations in this project, this $\Delta t = \frac{1}{100}$ attoseconds. All the particles in the simulation have their positions and velocities updated using Eqs. (2), (3), and (4) at every iteration of the simulation.

3 Monte Carlo

The second simulation type is a Monte Carlo simulation [5]. It is based on statistical physics using the electrostatic energy ($U_c = k_e \frac{q_1 q_2}{r_{1-2}}$) of each particle. The simulation is stochastic and we expect it to be statistically correct. For a particle P in a position i , we can find its electrostatic potential energy U_i with respect to all other particles:

$$U_c = \sum_{j=1}^N k_e \frac{q_P q_j}{r_{j \rightarrow P}} \quad (5)$$

The particle then makes a hypothetical, random movement to a new position f , at which we can find its new electrostatic potential energy U_f using Eq. (5). The magnitude of the random movement is based on the kinetic theory of matter, so the random movement is given by Eq. (4), using Eq. (1) to find the magnitude of \vec{v} . We then find the change in energy, $\Delta U = U_f - U_i$. If $\Delta U \leq 0$, then we accept the random movement, simulating the particle moving to a lower energy state. If the change is greater than zero, we then compare $e^{\frac{-\Delta U}{k_b T}}$ to R_n , where R_n is a random number between zero and one. The exponential function comes from the probability distribution of the possible states of our system as given by Boltzmann statistics [1]. If $e^{\frac{-\Delta U}{k_b T}} > R_n$, then we accept the random movement and the particle's new position is f . If not, then we reject the movement and the particle remains in the position i . For greater positive changes in energy, the exponential function decreases, and the probability of accepting the random movement becomes lower. This process is repeated for each particle in the simulation; thus, the ensemble of particles should eventually evolve into the lowest energy state. To ensure that this minimum energy state is the global minimum rather than a local minimum, if the particles remain in the same state for the duration of five consecutive measurements, every particle is given a random movement based on its statistical average speed; if the ensemble was in its lowest energy state, then it will quickly return to it, if not, the "jolt" enables the particles to attempt to move into a lower energy state.

4 Additional Calculations for Both Simulation Types

Additionally, we include the effects of the work function and the Pauli exclusion principle. The work function Φ is the minimum quantity of energy needed to remove an electron to a point immediately outside the metal [1]. In the PD simulation, we account for this by subtracting the work function from the kinetic energy KE of a particle as it crosses the top boundary of the simulation box. By the conservation of energy: $KE_f = KE_i - \Phi$, and since

$KE = \frac{1}{2}mv^2$, we find the final speed after the work function has been applied to be:

$$v_f = \sqrt{v_i^2 - \frac{2\Phi}{m}} \quad (6)$$

If $v_i^2 - \frac{2\Phi}{m} < 0$, the function is undefined using real numbers, so the velocity defaults to zero, indicating the particle does not have enough energy to escape, and it loses all its energy in the attempt. In the MC simulation, we simply add the work function to U_i if the particle has passed the surface of the metal, making the particle likely to reenter the metal.

To account for the Pauli exclusion principle when the electrons' wavefunctions begin to overlap each other, we construct an approximate function such that its repulsive potential U_r overpowers the Coulomb potential at close distances, and has no effect at large distances. There is no universally accepted method for describing the Pauli repulsion; it is sometimes approximated by r to some relatively large negative power (typically between -8 and -10) [1] although, the Lennard-Jones potential uses a repulsive term with a power of -12. Alternatively, it is approximated using an exponential function [6]. Here, we have chosen the latter approach:

$$U_r = \frac{a_0}{\alpha} e^{\alpha(r_{ion}-r)}, \quad (7)$$

where r is the distance between two interacting particles, r_{ion} is the ionic radius of the metal ions, and α is a constant equal to 1 \AA^{-1} , such that the argument of the exponential is unitless and the equation has units of energy. The constant a_0 describes the strength of the repulsion and can be found using the total potential energy U of a simple two-particle system: $U = U_c + U_r$. Because we treat the valence electrons as free, they should begin to overlap the remaining electrons around each ion and be repulsed at a distance equal to the ionic radius r_{ion} . Assuming equilibrium at a separation r_{ion} , the minimum value of U should occur at r_{ion} . We use the first derivative of U to find the value of a_0 such that this condition is satisfied. Also, since the potential due to Pauli exclusion is always repulsive, we take the absolute value, so the resulting value for a_0 is $k_e \frac{|q_1 q_2|}{r_{ion}^2}$.

In the MC simulation, we apply Eq. (7) when the distance between an ion and an electron is r_{ion} . As for the PD simulation, since force is the negative derivative of the potential energy function with respect to position [7], and because the degeneracy pressure is always repulsive, the effective force F_r due to the Pauli exclusion principle is the absolute value of the derivative with respect to position of Eq. (7):

$$F_r = \left| \frac{dU_r}{dr} \right| = a_0 e^{\alpha(r_{ion}-r)}. \quad (8)$$

By adding Eq. (8) to Eq. (2), for any particle j closer than the ionic radius to another ion, we find the net force on j due to both Coulomb and Pauli interactions. We then apply Newton's second law and the equations of motion to update the position of j .

5 Results

With the program, we obtain results from each simulation type for several trials. The distance between pairs of adjacent ions is measured and these measurements are averaged

together. The distances between particles oriented parallel to the metal surface and those oriented perpendicular to it are recorded separately. The change in average separation between neighboring ions is reported as a percentage difference from the original separation (the lattice constant). The measurements for these trials were taken every ten thousand iterations of the simulation. In each of these trials, the electron density drops from 100% (a balance of charge) to 50% (half of the electrons are removed) at the one-hundred thousandth iteration. The different trials are indicated by the difference in color and shape of the data points, the darker shade corresponds to the percent change in ion separation from the lattice constant parallel to the metal's surface and the lighter shade corresponds to the change perpendicular to the surface. For example, the two blue, diamond-shaped marker data sets are from the same trial, each representing a different set of measurements: the lighter set indicating the average separation change between adjacent ions aligned perpendicular to the metal surface, and the darker set indicating the same measurements for ions aligned parallel to the metal surface. The PD results are shown in Figure (3):

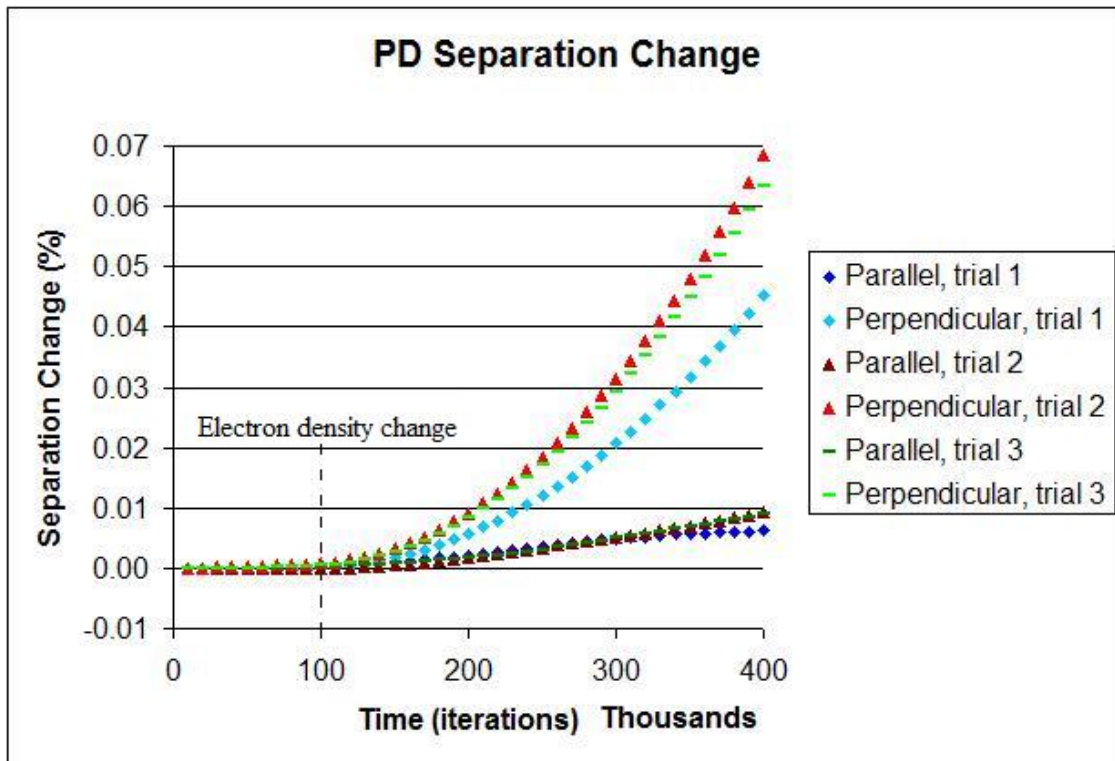


Figure 3: Three PD trial results showing the average change in separation between adjacent ions along directions perpendicular and parallel to the surface of the metal.

Using the PD simulation, we see the average separation of ions increases, as expected. Qualitatively, the largest separation appeared between the surface and second ion layers, and there were fewer electrons in this region than between the other layers.

To test the stability of the simulation, we run a trial where the electron density does not change (a “normal” trial, without an electric field). In this trial, we see a gradual increase in spacing as well; the reason for this is unclear at this time. However, if we compare trials with normal and changed electron densities, shown in Figure (4), we see the ions separate much more quickly in the trial where the electron density decreased. Because we are unsure of the cause of this gradual increase, we are hesitant to claim that this is a systematic error and simply subtract it from the results of a trial where the electron density does change.

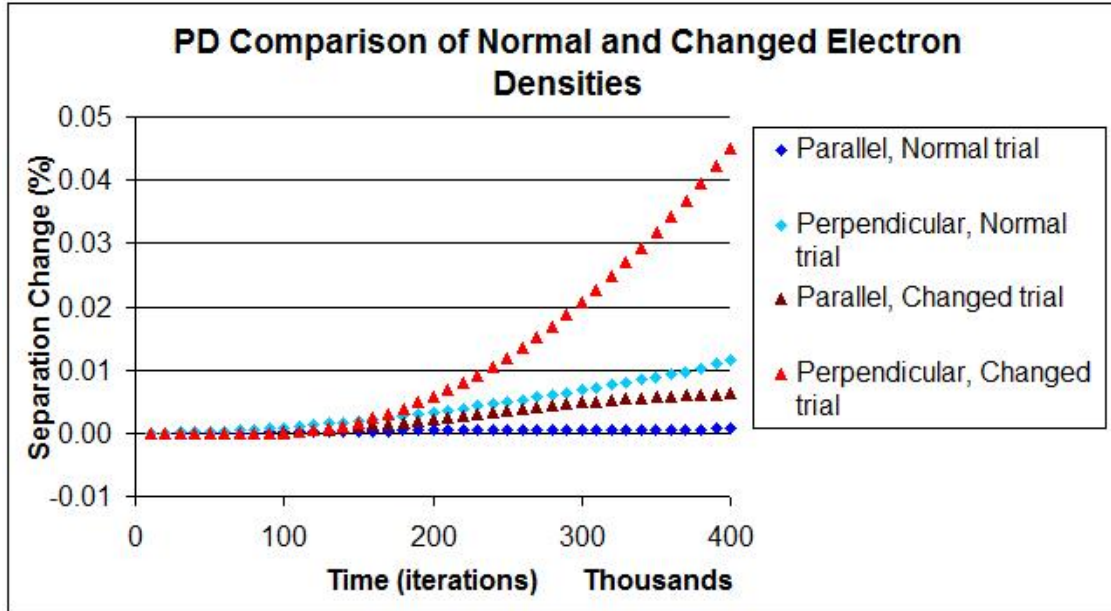


Figure 4: A comparison of PD trials for normal ($\rho = \rho_0$) and changed ($\rho = P\rho_0$) electron densities, showing the separation in adjacent ions arranged both perpendicular and parallel to the surface of the metal.

The changing separation witnessed in the constant electron density trial seems to imply that even under normal conditions, the ions tend to rearrange themselves on the surface: the lattice spacing increases, but the ions retain their location in the lattice. So, the surface of a metal has a less rigid crystal structure than simulated. The lower electron density only seems to expedite the surface deformation. Qualitatively, we see that the deformation largely occurs only in the first and second layers of ions.

For the MC trials, we use the same virtual experiment where the electron density drops from 100% to 50% at the one-hundred thousandth iteration, and measurements are taken every ten thousand iterations. The data is given in Figure (5):

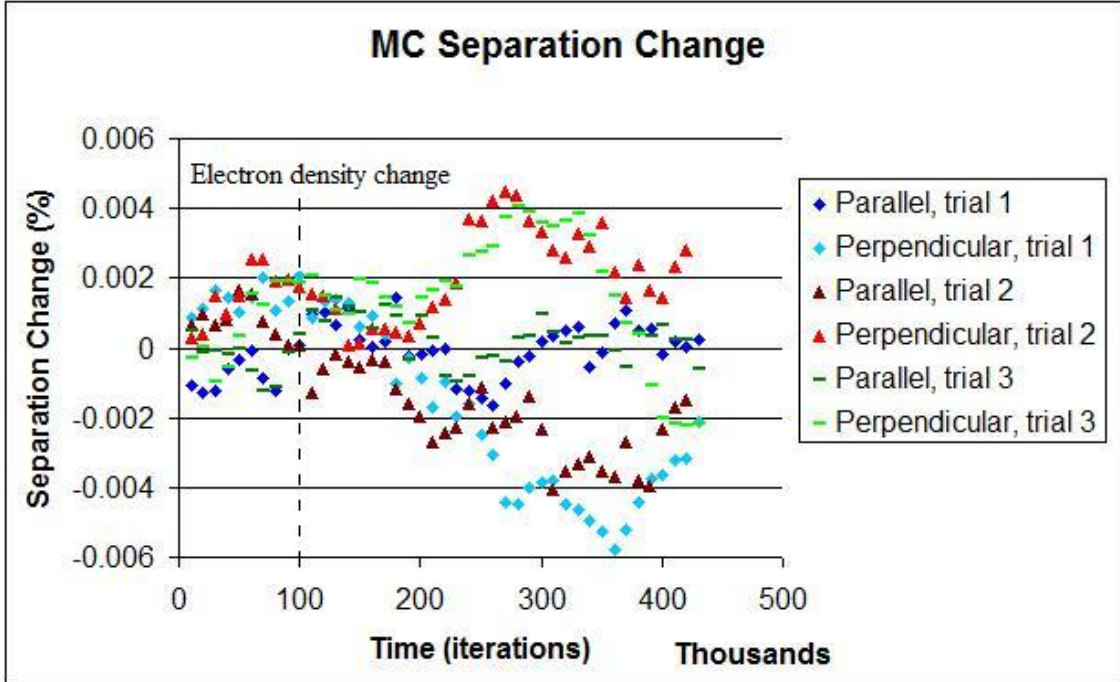


Figure 5: Three MC trial results showing the separation in adjacent ions arranged both perpendicular and parallel to the surface of the metal.

We expect the data to have a lot of variance because of the stochastic nature of the MC simulation. The only consistency between the trials seems to be that after the electron density drops, the ions are more free to move, causing a more pronounced change in separation, both in expansion and contraction. We see that even after the electron density drops, the average separation remains around its original value.

We also note that the scale of the change in separation in the MC simulation is much smaller than that given by the PD simulation. Comparing the two simulation types, the MC does not seem to be as strongly affected by a decrease in electron density as the PD simulation. Clearly, the PD simulation shows an increased rate of changing ion separation for the electron deficient surface of a single-element metal, and the MC simulation shows a comparatively smaller change.

6 Conclusion

In this project we have created a simulation for exploring surface structure of metals. Further research in this topic should include an examination of the crystal structure at the surface of the metal. We also suggest modifying the PD simulation such that it applies an electric field directly to the metal particles (both ions and electrons), rather than simulating the effect of a field using a decreased electron density. This would require a modification of the boundary conditions. It might also be appropriate to use a “graded-density” approach in which the initial electron density changes with depth from “depleted” ($\rho = P\rho_0$) at the

surface to “normal” ($\rho = \rho_0$) several layers of ions into the metal from the surface. We conclude that using the PD simulation has demonstrated the separation in ions expected at the electron-deficient surface of a metal. In fact, this separation not only increased, but the crystal structure of the metal began to break down. Using a MC simulation, we see little effect in decreasing the electron density, except for an increase in deviations from the original ion separation. We hope that we have demonstrated the usefulness of simulations such as this in exploring the atomic-scale behavior of different materials, metals in particular.

Acknowledgments

The author would like to acknowledge Jeremy Liberman for programming assistance. He would also like thank his anonymous reviewers at the Journal of Undergraduate Research in Physics for helpful suggestions. Finally, he would like to thank his advisor, Dr. James H. Taylor, for his support and guidance throughout the entire process of this research.

References

- [1] Kenneth Krane. *Modern Physics: Second Edition*. New York: John Wiley and Sons, 1996.
- [2] Roald K. Wangsness. *Electromagnetic Fields: Second Edition*. New York: John Wiley and Sons, 1979.
- [3] Tao Pang. *An Introduction to Computational Physics: Second Edition*. Cambridge: University Press, 2006.
- [4] J. M. Haile. *Molecular Dynamics Simulation*. New York: John Wiley and Sons, 1992.
- [5] David P. Landau and Kurt Binder. *A Guide to Monte Carlo Simulations in Statistical Physics*. Cambridge: University Press, 2005.
- [6] John J. Brehm and William J. Mullin. *Introduction to the Structure of Matter*. New York: John Wiley and Sons, 1989.
- [7] Paul A. Tipler and Gene Mosca. *Physics for Scientists and Engineers: Fifth Edition*. New York: W. H. Freeman and Company, 2004.